European Journal of Medicinal Chemistry Reports 18 (2026) 100376

Contents lists available at ScienceDirect

European Journal of Medicinal Chemistry Reports

journal homepage: www.editorialmanager.com/ejmcr/default.aspx

Design, synthesis, and biological evaluation of novel oxindole-based derivatives as potent and selective antileukemic agents.

Muhamad Mustafa [a,*], Aya Soudi [b], Petr Dzubak [c,d], Sona Gurska [c,d], Ivo Frydrych [c,d], Marian Hajduch [c,d], Burak Tüzün [e], Ibrahim M. Salem [f], Tarek S. Ibrahim [g,h], Michael Smietana [a], Jean-Yves Winum [a], Omar M. Aly [i], Taha F.S. Ali [b,**], El-Shimaa M.N. Abdelhafez [b,j]

[a] IBMM, Univ Montpellier, CNRS, ENSCM, Montpellier, France
[b] Department of Medicinal Chemistry, Faculty of Pharmacy, Minia University, Minia, 61519, Egypt
[c] Institute of Molecular and Translational Medicine, Faculty of Medicine and Dentistry, Palacký, University, Olomouc, Czech Republic
[d] Laboratory of Experimental Medicine, Institute of Molecular and Translational Medicine, University Hospital Olomouc, Olomouc, Czech Republic
[e] Plant and Animal Production Department, Technical Sciences Vocational School of Sivas, Sivas Cumhuriyet University, Sivas, 58140, Turkey
[f] Department of Pharmaceutical Chemistry, Faculty of Pharmacy, Sphinx University, New Assuit City, Assiut, 71515, Egypt
[g] Department of Pharmaceutical Chemistry, Faculty of Pharmacy, King Abdulaziz University, Jeddah, 21589, Saudi Arabia
[h] Department of Pharmaceutical Organic Chemistry, Faculty of Pharmacy, Zagazig University, Zagazig, 44519, Egypt
[i] Department of Medicinal Chemistry, Faculty of Pharmacy, Port Said University, Port Said, 42511, Egypt
[j] Medicinal Chemistry Department, Faculty of Pharmacy, Minia National University, New Minia, 61768, Egypt

ARTICLE INFO

Keywords:
Oxindole
Acute lymphoblastic leukemia
Anticancer
Molecular dynamics
VEGFR2
JAK3
FGFR1

ABSTRACT

Acute lymphoblastic leukemia (ALL) is an aggressive hematological malignancy that requires rapid therapeutic intervention. In this study, a series of oxindole-based derivatives (**5a-t**) was designed, synthesized, and evaluated for antiproliferative activity. Initial single-dose screening at the NCI-DTP identified five compounds for full five-dose evaluation. Among these, compound **5t** emerged as the most potent analogue, demonstrating broad antiproliferative activity across the NCI-60 panel with GI_{50} (MG-MID) values ranging from 9.05 to 45.24 μM and exhibiting pronounced selectivity toward leukemia cell lines. Compound **5t** showed superior cytotoxicity against CCRF-CEM cells while displaying markedly lower toxicity toward normal fibroblasts (BJ and MRC-5), yielding selectivity indices >17, thereby outperforming ibrutinib. Kinase profiling revealed that **5t** functions as a multi-kinase inhibitor, potently targeting JAK3, VEGFR2, and FGFR1, with sustained inhibition observed at low micromolar concentrations. Mechanistic studies further demonstrated dose-dependent S-phase accumulation, accompanied by a slight increase in the G2/M DNA-content fraction in CCRF-CEM cells, accompanied by a near-complete shutdown of bulk RNA and DNA synthesis by the most potent analogue **5o**. Complementary molecular modeling supported stable binding of **5t** to JAK3 and VEGFR2, while *in silico* ADME predictions indicated favorable oral drug-like properties. Collectively, these findings identify as a viable candidate for further preclinical evaluation for the development of new therapeutic agents against ALL.

1. Introduction

Acute lymphoblastic leukemia (ALL) is a hematologic malignancy characterized by uncontrolled proliferation of immature lymphoid cells and remains a major contributor to cancer related mortality despite substantial therapeutic progress over recent decades [1]. In 2019, approximately 5930 new cases of ALL were diagnosed in the United States and nearly 1500 patients died from the disease [2]. Although advances in risk-adapted, multi-agent chemotherapy and supportive care have raised survival rates in pediatric ALL to over 90% in high-income settings, therapeutic outcomes in adults remain markedly inferior. Disease relapse, the emergence of drug resistance, and treatment-associated toxicities continue to present major clinical challenges, particularly among adult, relapsed/refractory, and other

* Corresponding author.
** Corresponding author.
E-mail addresses: muhamad-mustafa.hussein@umontpellier.fr (M. Mustafa), taha.ali@mu.edu.eg (T.F.S. Ali).

https://doi.org/10.1016/j.ejmcr.2026.100376
Received 22 June 2026; Received in revised form 14 September 2026; Accepted 6 October 2026
Available online 7 October 2026
2772-4174/© 2026 The Authors. Published by Elsevier Masson SAS. This is an open access article under the CC BY license (http://creativecommons.org/licenses/by/4.0/).

high-risk subgroups [3]. These limitations underscore an urgent need for innovative therapeutic strategies capable of selectively targeting oncogenic signaling pathways essential for leukemic cell survival and proliferation.

Protein kinases (PKs) are central regulators of intracellular signal transduction, orchestrating phosphorylation-dependent that control fundamental cellular processes such as proliferation, differentiation and apoptosis [4]. Aberrant activation, dysregulation, or mutation of PKs contributes to the pathogenesis of numerous diseases, including many cancers, by disrupting physiologic signaling homeostasis. Owing to their pivotal role in cellular regulation, PKs have emerged as highly attractive drug targets. Small-molecule inhibition of ATP-dependent phosphorylation represents the predominant therapeutic strategy for modulating dysregulated PK-mediated pathways [4,5]. The approval of imatinib in 2001 by the U.S. Food and Drug Administration (FDA) marked a transformative milestone as the first clinically successful small-molecule protein kinase inhibitor (PKI), revolutionizing the treatment landscape for chronic myeloid leukemia and setting the foundation for a new era in targeted therapy. Since then, PKIs have been extensively investigated across diverse therapeutic fields, including oncology, immunology, inflammatory diseases, metabolic disorders, and neurodegeneration [6]. Currently, hundreds of PKIs are under evaluation in global clinical trials, and over 80 have been approved by the FDA-most for oncologic indications, underscoring their broad clinical relevance and therapeutic potential [7].

Janus kinase 3 (JAK3) is a non-receptor tyrosine kinase predominantly expressed in hematopoietic cells and plays a critical role in cytokine receptor signaling, especially in T cell development and differentiation [8]. Owing to its restricted expression within immune cells, JAK3 represents an attractive target for selective inhibition, offering therapeutic potential in various cancers as well as autoimmune disorders. JAK3 inhibitors exhibit immunosuppressive, anti-inflammatory, and anti-thrombotic activities and have demonstrated promising anti-leukemic effects in preclinical models [9]. Multiple studies have demonstrated that JAK3 inhibitors suppress leukemic cell proliferation and induce apoptosis, supporting their potential utility as anti-leukemic agents (tofacitinib **I**, Fig. 1) [10].

Vascular endothelial growth factor receptor 2 (VEGFR2) plays a key role in leukemic progression through its involvement in angiogenesis and remodeling of the bone marrow microenvironment. In acute leukemia, including ALL, VEGFR2 expression is significantly elevated in newly diagnosed and relapsed patients compared to those in remission [11]. In juvenile-ALL, VEGFR2 levels are markedly reduced at diagnosis but increase after post-induction therapy, suggesting that leukemic infiltration alters VEGFR2 expression, and that level returns to baseline following effective treatment [12]. Inhibiting VEGFR2 with agents such as Apatinib (**II**) has demonstrated promising outcomes in suppressing the growth and causing apoptosis of ALL cells (Fig. 1) [13]. Small molecule inhibitors directed against VEGFR2 have demonstrated effectiveness in preclinical models, indicating their potential use in the treatment of ALL [14].

In parallel, fibroblast growth factor receptors (FGFRs) constitute a family of receptor tyrosine kinases that regulates cell proliferation, migration, angiogenesis, and organ development [15]. Among these, FGFR1 has been particularly implicated in the development and progression of various leukemias, including T-ALL. The inhibition of FGFR1 has been show to suppress leukemic cell growth. However, emergence of resistance mechanisms remain a limitation, emphasizing the need for improved therapeutic strategies [16,17].

The oxindole (indolin-2-one) scaffold represents a privileged structural motif in kinase inhibitor design due to its capacity to interact with conserved ATP-binding residues across a broad spectrum of kinases [18]. Numerous oxindole-based derivatives have exhibited potent inhibitory activity against JAK3, VEGFR2, and FGFR1 (compound **III**, Fig. 1) [19–21]. In addition, several FDA-approved multi-kinase inhibitors, including SU4984 (**IV**), sunitinib (**V**), and nintedanib (**VI**), are built upon this core structure. Collectively, these precedents highlight the suitability of oxindoles for the development of rationally designed multi-kinase inhibitors with optimized selectivity profiles (Fig. 1).

Considering the multifactorial nature of leukemia signaling pathways, the development of multi-targeted kinase inhibitors capable of simultaneously modulating multiple oncogenic drivers represents a promising therapeutic approach. Accordingly, the design of compounds **5a-t** was guided by an analogue-based rational design and privileged

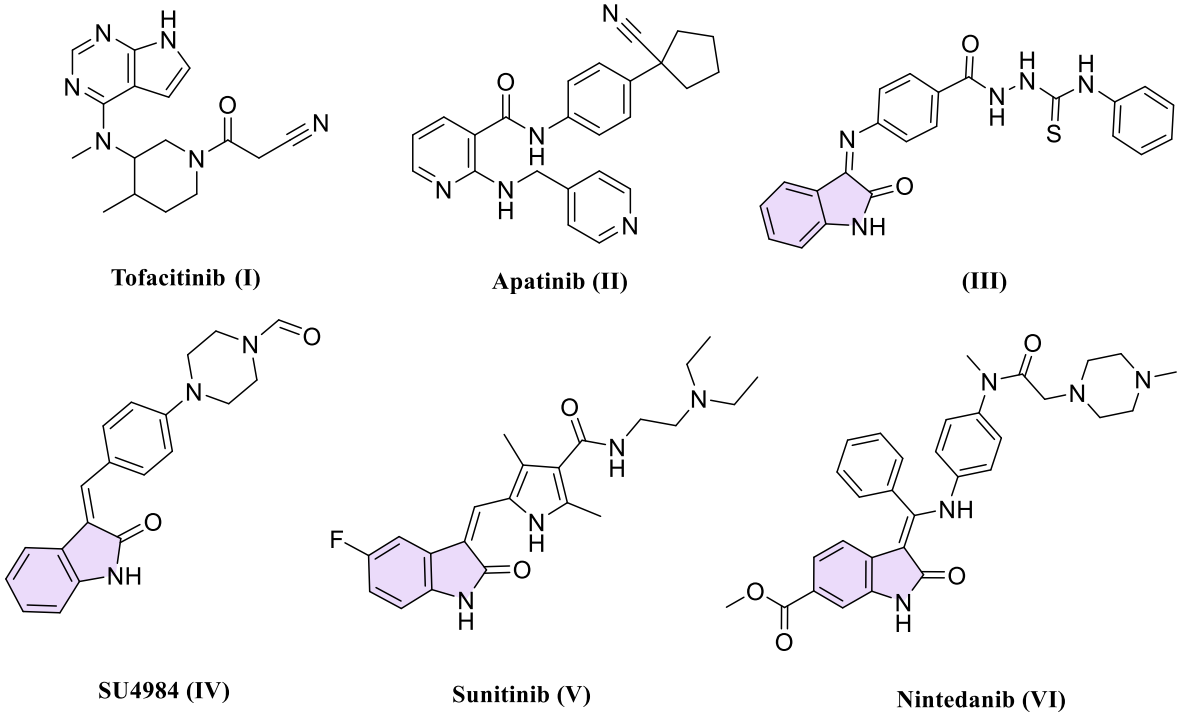


Fig. 1. Chemical structures of various tyrosine kinase inhibitors.

scaffold approach inspired by clinically validated oxindole-containing multikinase inhibitors, particularly sunitinib. The indolin-2-one nucleus was deliberately retained as the central hinge-binding pharmacophore, as its lactam NH and carbonyl groups furnish the classic complementary hydrogen-bond donor and acceptor motifs required for engaging conserved backbone residues in the kinase ATP-binding cleft. Structural diversity was systematically introduced across three optimization vectors: (i) halogen substitution on the oxindole core (H, 5-F, 5-Cl, or 6-Cl) to modulate electronic polarization and local halogen bonding; (ii) incorporation of *p*-hydroxybenzaldehyde- versus vanillin-derived central aromatic linkers to probe steric tolerance adjacent to the gatekeeper/ribose channel; and (iii) variation of the peripheral benzyl hydrophobic tail using 2-fluoro, 4-bromo, or 2-fluoro-4-bromo substituents to engage the adjacent hydrophobic cavity. This empirical strategy enabled a focused exploration of how steric occupancy, halogen positioning, and scaffold polarization collectively govern kinase affinity and antileukemic selectivity. Accordingly, the present study focuses on the design and synthesis of novel oxindole-based derivatives targeting JAK3, VEGFR2, and FGFR1, followed by comprehensive biological evaluation to assess their anti-leukemic potential.

2. Results and discussion

2.1. Chemistry

The synthetic route leading to the target compounds **5a-t** is depicted in Scheme 1. Initially alkylated *p*-hydroxy benzaldehyde derivatives or alkylated vanillin derivatives **3a-e** were obtained *via* S_N2 substitution reaction of various benzyl bromide derivatives **1a-e** and the nucleophilic phenolic hydroxyl group of vanillin or *p*-hydroxy benzaldehyde's nucleophilic hydroxyl group **2a-b**. The resulting intermediates **3a-e** subsequently underwent a base-catalyzed Knoevenagel condensation with the oxindole derivatives **4a-d** affording the final products **5a-t** in a good yield ranging from 55% to 89%. The newly synthesized compounds **5a-t** were characterized using a range of spectroscopic techniques. ^{1}H NMR of all target compounds displayed characteristic singlet signals at δ = 7.7-7.9 ppm corresponding to the ethylenic protons. In addition, NH protons appeared as singlet signals at δ = 9.83-10.74 ppm. A further singlet signal was consistently observed at range δ = 5.1-5.2 ppm attributed to methylene benzylic protons and at δ = 3.6-3.8 ppm for the OCH_3 protons found in compounds **5a-t**. Similarly, ^{13}C NMR confirmed the successful formation of the target scaffolds, showing the characteristic resonance of the ethylenic carbons at δ = 139-140 ppm, the aliphatic carbon at δ = 67.50-69.00 ppm and carbonyl carbons of CONH groups at δ = 159.37-163.09 ppm. All aromatic protons and carbons associated with the oxindole, phenyl, and benzyl moieties were fully consistent with the proposed structures of the synthesized compounds. The resulted compounds were a single *Z* isomer or a mixture of *E* and *Z* isomers and used without separation as reported earlier [22].

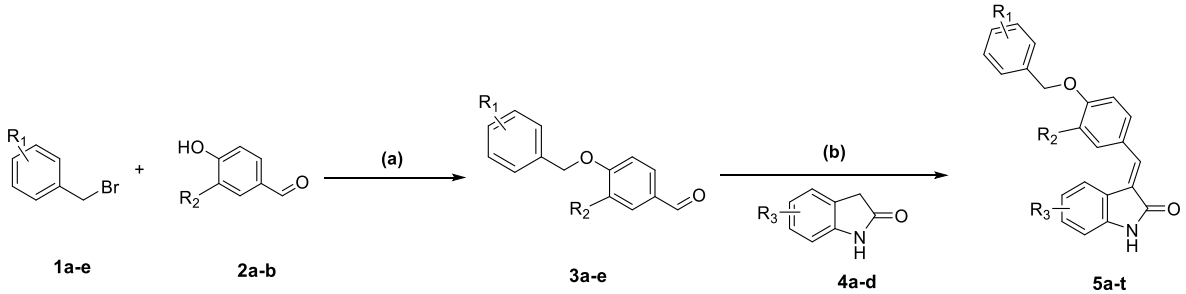
2.2. Biological evaluation

2.2.1. High throughput anti-cancer screening for compounds 5a-t

A panel of sixty human cancer cell lines from the National Cancer Institute (NCI) was used in an initial screening to evaluate the synthesized compounds (**5a-t**) at single dose concentrations (10^{-5} M) (see Table 1). Across all cell lines in the panel, Fig. 2 presents the mean growth-inhibition percentages (GI%) observed for the evaluated oxindole derivatives. All compounds demonstrated antiproliferative effects on the cell lines, and at micromolar concentrations, the majority of them inhibited tumor growth by more than half. Table 2 shows that at a concentration of 10 μM, six oxindole derivatives with a broad range of growth percentages had considerable growth inhibitory action, ranging from −54.97 to 194.86%. Compounds **5l** and **5t** exhibited cytotoxic effects with 46 and 7 cancer cell lines, respectively, when they were hybridized with 6-chloro oxindole as the hetero aromatic system, 2-fluoro-4-bromo benzyl bromide as the terminal hydrophobic tail, 4-hydroxybenzaldehyde or vanillin as the central aromatic linker. The antiproliferative action was significantly enhanced by compounds **5l** (mean % GI = 142.43) and **5t** (59.58). Using Vanillin and 4-bromo benzyl bromide moiety results in a loss of activity except for **5o** at a mean GI of 30.83% (see Fig. 3).

By keeping 4-hydroxybenzaldehyde as a central aromatic linker and hybridization of 6-chloro or 5-chloro oxindole with 4-bromo benzyl bromide moiety rather than the 2-fluoro-4-bromo benzyl bromide unit, also yielded compounds with measurable cytotoxic activity. Specifically, compounds **5h** and **5g** exhibited growth inhibitory effect across 34 and 43 cancer cell lines with mean GI of 115.39 and 124.43% respectively. On the other hand, replacement of 6-chloro oxindole (in case of compound **5l**) with 5-chloro oxindole in compound **5k** demonstrated superior activity with cytostatic effects towards 42 cell lines. Also, compounds **5i, 5j, 5f,** and **5o** showed cytostatic effect with 8, 8, 17, and 15 cancer cells, respectively.

Compounds **5g, 5h, 5k, 5l,** and **5t** showed growth inhibition in a single dose screen and advanced 5-dose [0.01-100 μM] testing against the full panel, demonstrating effectiveness against various tumor subpanel cells. Table 3 illustrates that compounds **5l** and **5g** showed promising cytotoxic activity against most tumor cell lines, with GI_{50} ranges of 1.46-20.50 μM and 1.45-25.2 μM, respectively. Additionally, compounds **5k, 5g,** and **5h** inhibited proliferation in 46, 54, and 55 cancer subpanel cell lines at single digit micromolar concentrations, respectively (Table 3). Compound **5t** exhibited substantial antiproliferative activity to nearly all tumor cell lines, with GI_{50} ranges of 2.12-100 μM (Table 3). Compounds **5g, 5h,** and **5l** showed a relatively consistent anti-proliferative effect across the NCI panel, with full panel GI_{50} (MG-MID) values of 3.74, 3.92, and 5.65 μM, respectively (Tables 4 and 5). The non-small cell lung cancer, CNS, and renal cancer subpanels were the most affected by **5l** (GI_{50} "MG-MID" = 3.09, 3.77, and 3.41 μM, respectively), (Table 5). Besides, SR, NCI-H522, SW-620, SNB 75, MELME-3M, OVCAR-4, UO-31, PC-3, and HS 575T cells were significantly inhibited by **5l** at low micromolar concentrations (GI_{50} = 2.72, 2.10, 2.50, 2.00, 2.76, 2.06, 1.36, 3.50, and 2.37 μM, respectively)



Scheme 1. Synthetic approach of compounds **5a-t**. Reagents and conditions: (a); K_2CO_3, ACN, reflux, 24 h; (b) Piperidine, EtOH, reflux, 3-6 h.

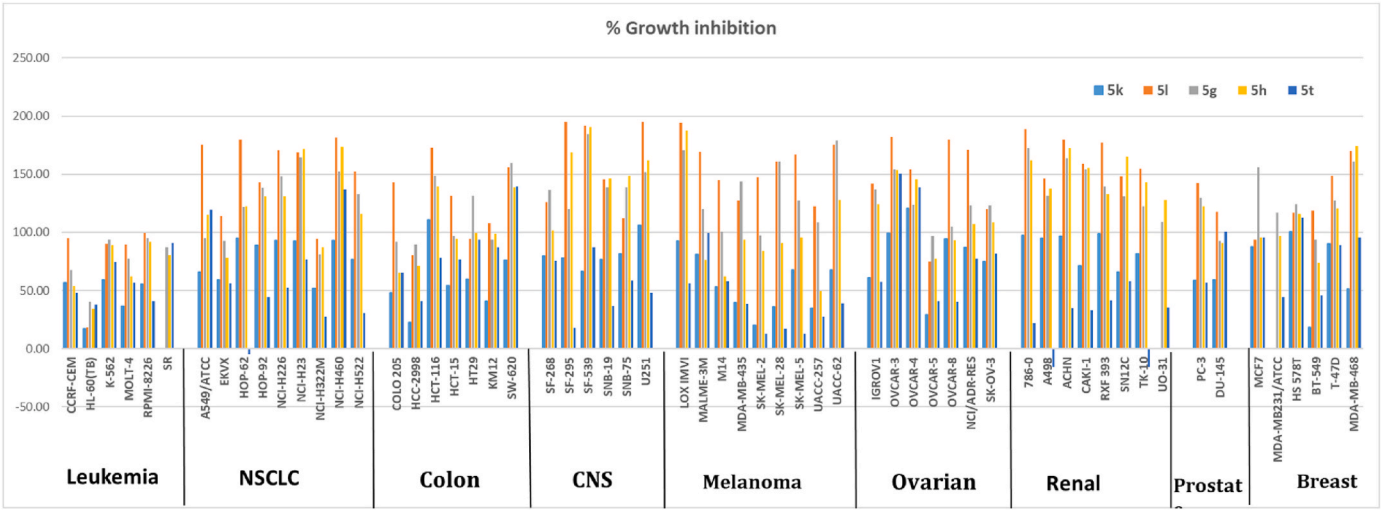


Fig. 2. % growth inhibition of compounds **5k**, **5l**, **5g**, **5h**, and **5t** over NCI 60 cell line panel.

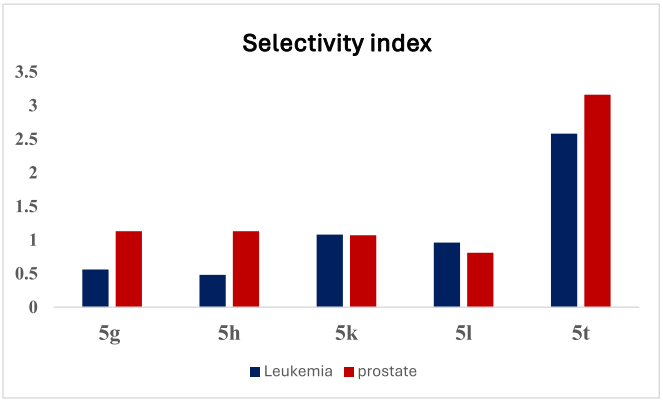


Fig. 3. Selectivity index of compounds **5g, 5h, 5k, 5l** and **5t** on leukemia and prostate cancer.

Table 1
Variable attachment points and substituents of the target compounds **5a-t**.

Cpd	R_1	R_2	R_3	Cpd	R_1	R_2	R_3
5a	2-F	H	H	**5k**	2-F 4-Br	H	5-Cl
5b	2-F	H	5-F	**5l**	2-F 4-Br	H	6-Cl
5c	2-F	H	5-Cl	**5m**	4-Br	OMe	H
5d	2-F	H	6-Cl	**5n**	4-Br	OMe	5-F
5e	4-Br	H	H	**5o**	4-Br	OMe	5-Cl
5f	4-Br	H	5-F	**5p**	4-Br	OMe	6-Cl
5g	4-Br	H	5-Cl	**5q**	2-F 4-Br	OMe	H
5h	4-Br	H	6-Cl	**5r**	2-F 4-Br	OMe	5-F
5i	2-F 4-Br	H	H	**5s**	2-F 4-Br	OMe	5-Cl
5j	2-F, 4-Br	H	5-F	**5t**	2-F 4-Br	OMe	6-Cl

(Table 3). Compound **5k** exhibited moderate anti-proliferative effect with GI_{50} (MG-MID) values ranging from 9.33 to 14.62 μM, in which leukemia was the most sensitive. However, compound **5k** inhibited cancer growth less than others. Compound **5t** exhibited anti-proliferative activity with GI_{50} (MG-MID) values ranging from 9.05 to 45.24 μM (Table 5). Concerning selectivity, compounds **5g**, **5h**, **5k**, and **5l** proved to be nonselective with broad spectrum anticancer activity against all tumor subpanels tested at GI_{50} level. Interestingly, **5t** has a high selectivity index on leukemia and prostate cancer with values equal to 2.55 and 3.16 μM (Fig. 2). Despite having the lowest mean growth inhibition value, compound **5t** was chosen for its potency and selectivity.

2.2.2. *Antiproliferative activity of compounds 5a-t*

The newly synthesized oxindole derivatives (**5a-t**) were tested against six human cancer cell lines to assess their *in vitro* cytotoxic IC_{50} values using ibrutinib as a reference drug. Besides, they were evaluated for their cytotoxic activity on two non-tumor fibroblast cells using the standard MTS test (Table 6) to validate their on-target activities and explore their safety profile. The cell lines included T-lymphoblastic leukemia (CCRF-CEM), myeloid leukemia (K562), solid tumors such as lung (A549) and colon (HCT-116, HCT-116p53-) carcinomas and osteosarcoma (U2OS). for comparison, two human non-cancer fibroblast cell lines (BJ, MRC-5) were also included in the study.

Compounds **5t** and **5o** exhibited the highest antiproliferative activity against all cancer cell lines as demonstrated by their IC_{50} values. Interestingly, compound **5t** and **5o** exhibited better activity on CCRF-CEM leukemic cell line (IC_{50} = 2.92 μM & 4.47 μM, respectively), than the reference ibrutinib (IC_{50} = 4.25 μM) (Table 5). Besides, **5n**, **5l**, and **5k** possessed moderate potency (IC_{50} = 10.39 μM - 12.17 μM), whereas the other derivatives possessed low potency (IC_{50} = 19.33 μM-29.49 μM). Furthermore, **5t** exhibited significant selectivity on CCRF-CEM cells compared to BJ and MRC-5 (IC_{50} > 50 μM, SI > 17.12) normal cell lines, respectively. In comparison, the reference drug ibrutinib exhibited IC_{50} values of 25.45 μM (SI = 6.5) and 27.56 μM (SI = 6.7) on the same normal cells, indicating that **5t** demonstrates significant activity, selectivity, and safety profiles. However, compound **5o** showed a lower IC_{50} value of 5.65 μM against MRC-5 cells (SI = 1.19) compared to ibrutinib, indicating reduced selectivity.

The synthesized compounds' IC_{50} values revealed a substantial ability of **5t**, **5l, 5o, 5n, 5h, 5a, 5g**, **5j**, and **5k** to inhibit A549 lung cancer growth; with IC_{50} values ranging from 6.72 μM to 25.50 μM which were superior to ibrutinib (IC_{50} = 29.35 μM). On the other hand, compounds **5b**, **5c**, and **5i** possessed moderate potency (IC_{50} = 31.52 μM- 43.55 μM). Besides, **5l** exhibited promising anti-proliferative activity on HCT-116 and HCT-116/P53/-, cells, with IC_{50} value of 5.74 μM and 5.52 μM, respectively, whereas reasonable selectivity was observed on BJ and MRC-5 normal cells, compared to ibrutinib.

Data analysis revealed that compounds **5b**, **5d, 5e, 5f, 5m, 5p, 5q, 5r,** and **5s** exhibited cytotoxic effects against most cancer cell lines, demonstrating IC_{50} values comparable to or lower than those of the reference drug while displaying no cytotoxicity towards normal cell lines. For instance, compounds **5m**, **5d**, and **5b** exhibited anti-proliferative effects on CCRF-CEM cell line, with IC_{50} values of 25.71, 25.66 and 25.51 μM, respectively. Compound **5h** demonstrated high potency against HCT-116, HCT-116/P53-, and U2OS cell lines, with IC_{50}

Table 2
Overview of the preliminary anticancer assay at single dose concentration of 10 μM.

Cpd.	Mean growth inhibition	Range of growth inhibition on all cells	The most sensitive cell lines	Positive cytostatic effect[b]	Positive cytotoxic effect[c]	No. of sensitive cell lines/Total cell lines
5a	16.12	−27.23[a] to 46.35	-	0/60	0/60	0/60
5b	20.94	−23.21[a] to 57.59	MCF7	3/56	0/56	3/56
5c	17.90	−19.98[a] to 66.08	MCF7	3/58	0/58	3/58
5d	11.43	−33.46[a] to 47.86	-	0/56	0/56	0/56
5e	4.75	−35.22[a] to 37.56	-	0/60	0/60	0/60
5f	41.20	−19.48[a] to 126.73	OVCAR-4	17/60	3/60	20/60
5g	124.43	40.09 to 184.26	SF-539	16/60	43/60	59/60
5h	115.39	34.34 to 190.46	SF-539	24/60	34/60	58/60
5i	34.64	−9.43[a] to 89.60	MOLT-4	8/57	0/57	8/57
5j	31.03	−11.37[a] to 64.52	NCI-H226	8/57	0/57	8/57
5k	69.71	16.84 to 120.46	OVCAR-4	42/57	4/57	46/57
5l	142.43	18.55 to 194.86	SF-295	9/57	46/57	55/57
5m	0.77	−54.97[a] to 34.31	-	0/59	0/59	0/59
5n	4.81	−41.11[a] to 46.14	-	0/59	0/59	0/59
5o	30.83	−39.96[a] to 84.73	ACHN	15/59	0/59	15/59
5p	11.09	−44.38[a] to 53.14	MCF7	1/58	0/58	1/58
5q	7.06	−18.21[a] to 39.66	-	0/57	0/57	0/57
5r	−1.65	−38.05[a] to 17.23	-	0/60	0/60	0/60
5s	3.88	−27.18[a] to 24.82	-	0/57	0/57	0/57
5t	59.58	−15.98[a] to 150.67	OVCAR-3	25/60	7/60	32/60

a Negative (−) indicates the cell killed. [b] the ratio between number of cell lines with percent growth from 0 to 50and total number of cell lines. [c] the ratio between number of cell lines with percent growth of <0 and total number of cell lines.

values recorded at 9.44, 5.54, and 7.31 μM, respectively.

2.2.3. Kinase profiling

We performed a primary *in vitro* kinase screen of compound **5t** against 18 recombinant kinases to establish a preliminary selectivity and activity profile. Compound **5t** demonstrated a clear differential inhibition pattern across the tested kinase panel. The strongest effects were observed at 10 μM, where JAK3, VEGFR2, and FGFR1 showed potent inhibition exceeding ~88–91% (Fig. 4). These kinases also retained measurable inhibition at 1 μM, with JAK3 showing the most persistent activity (~67% inhibition), whereas VEGFR2 and FGFR1 showed moderate reductions with ~30-50% inhibition. This pattern suggests a relatively high biochemical affinity of **5t** toward these targets. The strong reduction of JAK3 activity at both 10 μM and 1 μM positions JAK3 as the most likely biologically relevant target among the tested enzymes. On the other hand, SRC, GSK3β, KIT, and ABL1 exhibited moderate inhibition at 10 μM, typically within the range of 40–60% inhibition. At 1 μM, these effects dropped substantially, with most showing <20% inhibition, indicating lower binding affinity. The reduced inhibition of ABL1 at 1 μM, compared to more potent JAK3 inhibition, highlights a degree of selectivity that may be advantageous for targeted optimization. Overall, the biochemical profile indicates that compound **5t** functions as a selective multi-kinase inhibitor with preferential potency toward JAK3, complemented by notable activity against VEGFR2 and FGFR1. So, these findings further support the notion that **5t** displays preferential selectivity rather than promiscuous broad-spectrum inhibition.

2.2.4. Effect of the oxindole derivatives 5o and 5t on cell cycle modulation and DNA/RNA synthesis in CCRF-CEM cells

Compounds **5o** and **5t** were further evaluated in CCRF-CEM cells to test their effects on cell-cycle distribution (propidium iodide DNA-content analysis), on the mitotic marker phospho histone H3 (Ser^{10}), and on global DNA and RNA synthesis (BrdU/BrU pulse labeling) at 1 × and 5 × IC_{50}. Cell cycle profiles showed that dominant effect of both compounds was an accumulation of cells in S phase at the expense of G1 (Fig. 5). The effect was concentration dependent and most pronounced for **5o**, which decreased the G1 fraction from 39% in untreated cells to 25% at 5 × IC_{50} and expanded the S phase fraction from 45% to 57%. Compound **5t** produced a milder S phase delay accompanied by a modest increase of the G2/M population (from 15% to 17% at 5 × IC_{50}). The mitotic marker pH3-Ser^{10} was only marginally elevated above the control level across treated samples, indicating that the G2/M increment reflects a G2 accumulation rather than a true mitotic arrest. This is consistent with the expected upstream action of multi-kinase inhibitors that perturb mitogenic signaling and the intra-S/G2 checkpoints rather than the mitotic machinery itself.

These two compounds differed in the BrU/BrdU analysis, which showed an impact on transcription and replication, respectively. At 1 × IC_{50} both compounds produced a small increase of BrU+ and BrdU + cells, consistent with the early S-phase accumulation observed in panel A. At 5 × IC_{50}, however, compound **5o** showed a pronounced decrease of both RNA synthesis (BrU+: 33.6% to 17.1%) and DNA synthesis (BrdU+: 37.6% to 13.2%), reflecting a shutdown of biosynthetic activity and a transition from cytostatic to cytotoxic behavior. In contrast, compound **5t** at 5 × IC_{50} maintained an even higher fraction of RNA and DNA synthesizing cells (BrU+: 57.9%; BrdU+: 58.0%). This pattern is consistent with a predominantly cytostatic S-phase delay for **5t**, whereas **5o** acts as a more aggressive replication and transcription blocking agent at 5 × concentrations.

Taken together, the cell-cycle, mitotic and nucleic-acid-synthesis data are mutually consistent and fit the expected regulation for VEGFR2/FGFR1/JAK3-targeted oxindoles: interruption of mitogenic kinase signaling slows G1 to S progression and drives accumulation of cells in S phase with only a slight G2 spill-over and no true mitotic arrest, and higher exposure to the most potent analogue **5o** does significant shut down of RNA and DNA synthesis. These findings reinforce the declared mechanism of the antileukemic activity of the lead oxindole derivatives.

2.3. In silico study

2.3.1. Molecular docking

To obtain a more accurate molecular level validation of the observed biological activities, the predicted docking poses of compound **5t** within the active sites of VEGFR2 (PDB ID: 4AGD) [23], FGFR1 (PDB ID: 5A46) [24], and JAK3 (PDB ID: 7UYV) [25] were analyzed in comparison with their corresponding co-crystallized native ligands. The docking protocol was first validated by redocking the co-crystallized ligands: 1) Sunitinib into the active site of VEGFR (RMSD = 1.6167 Å), 2) Dovitinib into the active site of FGFR1 (RMSD = 1.9613 Å), and 3) OV5 into the active site of JAK3 (RMSD = 0.9429 Å), (**supplementary** data Fig. S1).

Table 3
NCI *in vitro* testing results of GI_{50} of compounds **5g, 5h, 5k,5l,** and **5t.**

Subpanel/tumor cell lines	Compound				
	5g	5h	5k	5l	5t
	GI_{50}(μM)	GI_{50}(μM)	GI_{50}(μM)	GI_{50}(μM)	GI_{50}(μM)
Leukemia					
CCRF-CEM	>10.00	**6.43**	4.55	3.86	14.40
HL60(TB)	>10.00	25.2	10.9	17.70	14.20
K-562	**3.46**	4.55	3.57	4.03	5.59
MOLT-4	6.50	4.95	4.63	3.98	6.36
RPMI-5226	3.95	4.27	9.01	4.41	22.20
SR	4.00	**3.90**	2.72	2.07	**3.96**
Non-small cell lung cancer					
A549/ATCC	**2.37**	**2.02**	3.25	2.08	**2.12**
EKVX	7.92	3.52	NT	3.69	52.20
HOP-62	**2.45**	**2.36**	4.51	1.90	15.40
HOP-92	**1.62**	**2.03**	3.14	2.28	13.30
NCI-H226	**1.52**	**1.45**	2.12	2.07	43.60
NCI-H23	**1.50**	**1.74**	2.66	1.79	12.50
NCI-H322M	**2.52**	3.56	2.95	4.43	39.50
NCI-H460	3.43	**2.17**	3.50	2.02	14.50
NCI-H522	**1.74**	**1.93**	2.10	1.99	14.70
Colon cancer					
COLO 205	6.23	4.52	9.15	4.03	24.50
HCC-2995	**3.15**	6.15	20.50	15.40	25.40
HCT-116	**2.47**	**2.35**	3.13	1.93	10.60
HCT-15	>10.00	13.30	5.77	3.40	>100.00
HT29	**2.76**	**3.64**	12.9	4.69	9.14
KM12	>10.00	7.90	5.56	3.54	55.00
SW-620	**2.53**	**2.71**	2.50	2.02	4.36
CNS cancer					
SF-265	**2.97**	**3.76**	5.01	2.68	30.50
SF-295	**3.63**	**1.54**	3.25	2.07	>100.00
SF-539	**1.91**	**1.50**	6.32	1.92	23.00
SNB-19	**3.40**	**2.67**	4.06	2.30	34.30
SNB-75	**1.15**	**1.92**	2.00	2.19	19.00
U251	**1.97**	**1.76**	2.03	1.92	5.04
Melanoma					
LOX IMVI	**2.55**	**1.55**	2.55	1.73	19.30
MELME-3M	**2.07**	**4.14**	2.76	1.82	19.60
M14	4.42	6.05	4.97	2.91	56.50
MDA-MB-435	4.17	6.55	9.51	2.87	33.10
SK-MEL-2	**2.10**	**2.76**	15.5	7.22	55.20
SK-MEL-25	**2.44**	**3.00**	5.42	2.18	35.30
SK-MEL-5	**2.56**	**3.17**	10.5	3.47	54.70
UACC-257	3.97	5.94	13.0	9.42	>100.00
UACC-62	**1.70**	**1.79**	3.72	1.82	24.50
Ovarian cancer					
IGROV1	**2.21**	**3.32**	4.11	2.43	15.90
OVCAR-3	**2.73**	**2.26**	3.25	2.49	14.50
OVCAR-4	**2.51**	**2.23**	2.06	1.90	**2.56**
OVCAR-5	5.05	4.03	13.00	8.24	23.50
OVCAR-5	**2.41**	**2.21**	3.74	3.31	13.50
NCI/ADR-RES	**3.03**	**2.36**	ND	-	9.99
SK-OV-3	**3.45**	**3.29**	4.20	3.81	53.70
Renal cancer					
756-0	**3.63**	**2.16**	3.06	1.90	39.10
A495	>10.00	**2.44**	2.45	2.23	>100.00
ACHN	**2.92**	**2.24**	2.19	1.92	>100.00
CAKI-1	**2.63**	**2.17**	2.05	1.70	45.70
RXF393	**2.47**	**1.91**	4.73	2.73	51.60
SN12C	**3.77**	**2.06**	4.62	5.31	39.00
TK-10	4.07	**2.73**	6.75	2.73	34.30
UO-31	**2.56**	**1.57**	1.46	1.55	30.70
Prostate cancer					
PC-3	**2.91**	**2.61**	3.50	1.91	10.20
DU-145	**3.70**	4.32	10.20	3.39	7.96
Breast cancer					
MCF7	4.25	9.25	2.95	2.11	10.20
MDA-MB-231/ ATCC	**2.25**	**2.24**	3.21	2.33	17.00
HS 575T	**2.57**	**2.31**	2.37	2.05	15.50
BT-549	**2.53**	7.17	9.45	1.92	41.10

Table 4
Median growth inhibitory concentrations[a] (GI_{50}, μM) of *in vitro* subpanel tumor cell lines for compounds **5g, 5h** and **5k**.

Subpanel tumor cell line	5g		5h		5k	
	MG-MID	Selectivity index	MG-MID	Selectivity index	MG-MID	Selectivity index
Leukemia	6.71	0.56	5.22	0.45	11.05	1.05
NSCL cancer	2.56	1.31	2.35	1.65	12.69	0.94
Colon cancer	5.49	0.65	5.54	0.67	10.63	1.12
CNS cancer	2.51	1.49	2.29	1.72	14.62	0.52
Melanoma	2.92	1.25	3.59	1.01	11.51	1.01
Ovarian cancer	3.10	1.21	2.51	1.40	13.33	0.59
Renal cancer	4.13	0.91	2.20	1.75	13.07	0.92
Prostate cancer	3.31	1.13	3.47	1.13	11.15	1.07
Breast cancer	2.64	1.42	4.24	0.92	9.33	1.25
Full panel MG-MID[a]	**3.10**		**3.20**		**4.50**	

Table 5
Median growth inhibitory concentrations[a] (GI_{50}, μM) of *in vitro* subpanel tumor cell lines for compounds **5l** and **5t**.

Subpanel tumor cell line	5l		5t	
	MG-MID	Selectivity index	MG-MID	Selectivity index
Leukemia	5.94	0.96	11.12	**2.55**
NSCL cancer	3.09	1.54	26.42	1.09
Colon cancer	5.97	0.63	32.71	0.55
CNS cancer	3.77	1.50	35.31	0.51
Melanoma	7.65	0.74	45.24	0.59
Ovarian cancer	5.07	1.12	19.56	1.47
Renal cancer	3.41	1.66	59.15	0.45
Prostate cancer	7.00	0.51	9.05	**3.16**
Breast cancer	6.22	0.91	16.42	1.74
Full panel MG-MID[a]	**2.55**		**21.40**	

Median value calculated according to the data obtained from NCI's *in vitro* disease-oriented human tumor cell screen. [a] GI_{50} (μM) full panel mean-graph midpoint (MG-MID) = the average sensitivity of all cell lines toward the test agents.

2.3.1.1. Molecular docking of compound 5t inside VEGFR active site. The rationale for exploiting selective VEGFR inhibitor that targets the aspartate-phenylalanine-glycine (DFG_{out}) conformation is supported in ligand binding within the regulatory domain pocket (RDP), distal to the conserved regions of the ATP-binding site [26,27]. Within the adenine-binding site, largely nonselective interactions are conserved across kinases and are therefore accommodated by most ATP-competitive inhibitors. Each VEGFR2 TK inhibitor should contain a heterocyclic moiety that positions a hydrogen-bond acceptor toward the backbone donor, accompanied by hydrogen-bond donor interaction, as exemplified by sunitinib [23]. The binding mode of compound **5t** within the active site of VEGFR2 was investigated and compared with that of the co-crystallized native ligand sunitinib, as illustrated in (Fig. 6). The two-dimensional and three-dimensional interaction maps (Fig. 6 $A_{1,2}$ & $B_{1,2}$) reveal that compound **5t** establishes a network of key intermolecular interactions that closely resemble those formed by sunitinib, suggesting a comparable binding pattern within the VEGFR2 catalytic pocket. Both compounds **5t** and sunitinib revealed three crucial contacts within the VEGFR (RDP): 1) π-π* stacking with the key DFT (Phe1047) residue with bond lengths of (5.05 Å for **5t**) and (5.38 Å for sunitinib), 2) H-bonding donor effect due to the indole-NH with the Glu917 (2.14 Å

Table 6
Cytotoxic activities of the oxindole derivatives **5a-t** against six tumor and two normal fibroblast cell lines.

Comp.	IC_{50} ± SD (μM)							
	A549	CCRF-CEM	HCT116	HCT116P53-	K562	U2OS	BJ	MRC-5
5a	24.62 ± 1.25	19.33 ± 1.24	33.52 ± 6.70	32.06 ± 6.25	24.25 ± 3.56	34.12 ± 3.91	ND	ND
5b	41.25 ± 3.50	25.51 ± 2.92	>50	>50	>50	>50	>50	>50
5c	31.52 ± 3.55	19.76 ± 2.26	36.01 ± 6.53	34.52 ± 6.17	27.74 ± 2.05	32.05 ± 2.16	34.17 ± 3.66	31.13 ± 4.73
5d	>50	25.66 ± 4.52	>50	>50	>50	>50	>50	>50
5e	>50	>50	>50	>50	>50	>50	>50	>50
5f	>50	>50	>50	>50	>50	>50	>50	>50
5g	25.50 ± 3.92	29.49 ± 4.73	25.25 ± 3.52	21.55 ± 3.42	26.77 ± 4.93	24.51 ± 6.53	>50	31.50 ± 5.55
5h	9.34 ± 1.32	22.97 ± 2.41	9.44 ± 1.25	5.54 ± 1.67	23.45 ± 3.23	7.31 ± 1.50	ND	12.45 ± 2.29
5i	43.55 ± 4.64	25.94 ± 4.65	>50	>50	ND	30.95 ± 7.03	ND	ND
5j	25.55 ± 4.15	19.55 ± 2.35	36.52 ± 4.64	31.63 ± 3.95	25.67 ± 3.73	25.62 ± 3.16	ND	31.57 ± 6.23
5k	26.06 ± 4.25	12.17 ± 1.31	32.00 ± 3.27	31.17 ± 1.53	15.3 ± 2.59	25.36 ± 3.34	29.26 ± 1.54	17.01 ± 4.66
5l	6.39 ± 0.65	10.39 ± 0. 54	5.74 ± 1.03	5.52 ± 1.72	11.40 ± 1.12	4.56 ± 0.65	11.05 ± 1.01	5.20 ± 0.36
5m	>50	25.71 ± 5.43	>50	>50	>50	>50	>50	>50
5n	13.61 ± 2.72	11.34 ± 1.56	ND	29.90 ± 6.40	29.32 ± 6.61	17.43 ± 3.52	27.42 ± 4.67	ND
5o	7.57 ± 0.57	4.47 ± 0.66	10.14 ± 2.00	5.96 ± 1.95	17.52 ± 2.10	6.46 ± 1.29	ND	5.65 ± 0.70
5p	>50	ND	>50	>50	>50	>50	>50	>50
5q	>50	ND	>50	>50	>50	>50	>50	>50
5r	>50	>50	>50	>50	>50	>50	>50	>50
5s	>50	>50	>50	>50	>50	>50	>50	>50
5t	6.72 ± 0.27	2.92 ± 0.57	9.55 ± 1.63	7.30 ± 1.23	7.64 ± 1.59	6.70 ± 0.70	>50	>50
Ibrutinib	29.35 ± 3.40	4.25 ± 0.93	27.36 ± 3.24	29.55 ± 0.65	29.54 ± 0.55	22.61 ± 3.06	25.45 ± 1.23	27.56 ± 0.45

ND = not determined.
SI= Selectivity index for cancer cell which was calculated as follows: cancer cell selectivity index = IC_{50} (normal cell)/IC_{50}(cancer cell).

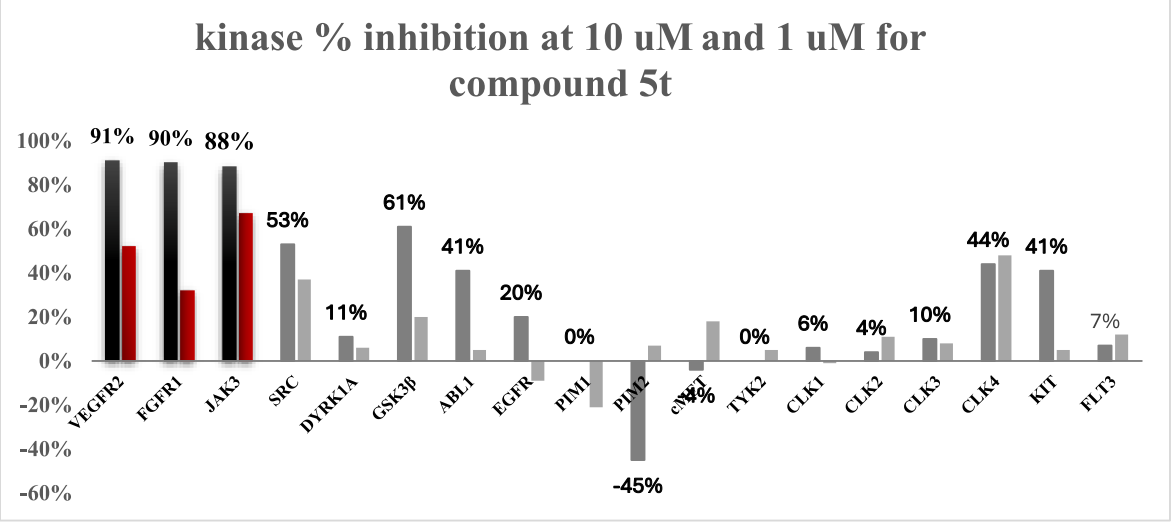


Fig. 4. Inhibition percentages of a selected kinase panel by compound **5t** at two concentrations 10 μM and 1 μM.

for **5t**) and (2.02 Å for sunitinib), 3) H-bonding acceptor effect due the carbonyl oxygen with the Cys919 residue (1.92 Å for **5t**) and (1.82 Å for sunitinib), implying that the compound may act as a competitive inhibitor by mimicking the native ligand's binding behavior. Conspicuously, compound **5t** occupies the ATP-binding cleft in a favorable orientation, enabling effective engagement with critical Asp1046 residue that lines the kinase channel and offers substantial opportunities for direct VEGFR-TK inhibitor interactions, thereby conferring distinct selectivity advantages [23]. Surface representation analysis (Fig. 6C_1 & C_2) highlights the deep insertion of compound **5t** into the VEGFR binding pocket, where it is enveloped by the protein surface in a manner comparable to sunitinib. This surface-bound conformation underscores the favorable steric fit and suggests enhanced ligand-protein interactions, which may contribute to improved binding affinity and inhibitory potential. Overall, the docking results suggest that compound **5t** exhibits a strong binding affinity toward VEGFR2 by adopting a stable conformation within the active site and engaging key residues similarly to the native ligand sunitinib, reinforcing the hypothesis that compound **5t** can effectively exploit the same pharmacophoric features essential for VEGFR inhibition, that require further optimization and experimental validation.

2.3.1.2. Molecular docking of compound 5t inside FGFR active site. Protein tyrosine kinases vary considerably in their propensity to undergo conformational rearrangements of the N-terminal DFG motif within the activation loop [28]. Some kinases, including FGFR1, appear resistant to this so-called "DFG flip" [24]. Nevertheless, the reference inhibitor dovitinib has unexpectedly been shown to inhibit FGFR1 *via* stabilizing the kinase in a DFG-out conformation [29]. After redocking of the dovitinib native ligand and the investigated compound **5t** inside the FGFR1 active site, the binding scoring of both is interestingly comparable (S = −8.690 kcal/mol, for dovitinib) and (S = −8.456 kcal/mol, for **5t**). The docking outcomes illustrated at (Fig. 7), clarified a conserved mode of recognition within the ATP-binding site. Dovitinib contacted the hinge region residues, Glu562 (H-bond donor, using 2-pyridone NH, 2.38 Å) and Ala564 (H-bond acceptor, using 2-pyridone

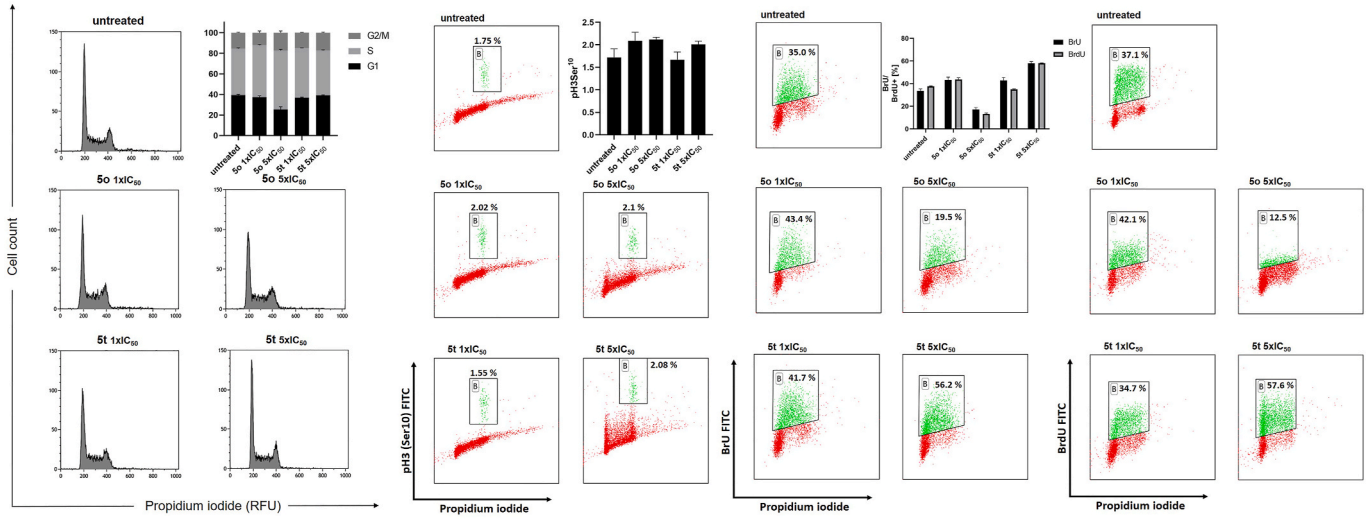


Fig. 5. Flow cytometry-based analysis of cell cycle distribution, histone levels, and nucleic acid synthesis. Data were acquired using a FACSCalibur flow cytometer (BD) and analyzed with Kaluza software (Beckman Coulter). (A) Cell cycle analysis. Representative DNA content histograms are shown (lower panel), illustrating the distribution of cells across different phases of the cell cycle. Corresponding quantification of cell populations in individual phases (e.g., G0/G1, S, G2/M) is presented as bar graphs (upper panel). (B) Histone marker analysis. Representative dot plots demonstrating the applied gating strategy and analyzed cell populations are shown (lower panel), with corresponding quantification of signal intensity displayed as bar graphs (upper panel). (C) RNA and (D) DNA synthesis analysis. Representative dot plots illustrating the detection of RNA and DNA synthesis, as well as their combined assessment, are shown (middle and lower panel). Quantitative analysis is presented as bar graphs (upper panel). All bar graphs represent mean values ± standard deviation (SD) derived from at least three independent experiments (n = 3).

carbonyl oxygen, 1.90 Å) and (H-bond donor, using benzimidazole NH, 2.12 Å) (Fig. 7 A_1, B_1 & C_1). Similarly, compound **5t** achieved two substantial intermolecular interactions: 1) H-bond donor with Glu562, using 2-oxoindole NH, 2.01 Å, and 2) H-bond acceptor with Ala564, using carbonyl oxygen of 2-oxoindole, 1.98 Å. In addition, compound **5t** achieved more favorable binding at hinge region, through combining the Lys514 residue by halogen effect due to chloro-substituent (2.24 Å) (Fig. 7 A_2, B_2 & C_2). The overlay with **5t** highlights a comparable positioning of the core scaffold within the binding pocket, suggesting that it effectively exploits key pharmacophoric features required for FGFR1 inhibition. To conclude, the ability of compound **5t** to engage key residues within the ATP-binding site provides a structural basis for its observed biological activity and supports its further development as a promising FGFR1-targeted tyrosine kinase inhibitor.

2.3.1.3. Molecular docking of compound 5t inside JAK3 active site. JAK3 is a member of the JAK family that mediates signaling from multiple cytokine receptors, as well as from growth hormone and erythropoietin [30]. Structure-based design of JAK3 inhibitors requires a molecular scaffold incorporating a hinge-binding motif that enables optimal vector orientations for substituent placement, thereby enhancing both potency and selectivity [25]. To validate, we compare the suitable placement of compound **5t** with the native 2-pyrrolone pyridine ligand (OV5) inside the hinge region of the ATP-binding domain of JAK3 (Fig. 8). Compound OV5 achieved two distinct water-bridged hydrogen bonding with H_2O1361 (1.91 Å) and H_2O1371 (1.95 Å), utilizing its carboxamide oxygen. Besides, it accommodates the hinge region Leu905 residue using 2-pyrrolone oxygen (2.17 Å) along with obvious insertion of its halo phenyl moiety inside a hydrophobic cavity (Fig. 8 A_1, B_1 & C_1). Regarding compound **5t**, it was proved to bind at the same region with a comparable anchoring of its halo benzyl group inside a similar hydrophobic pocket. In addition, it conferred two halogen effects due to bromo-substituent with His917 residue (3.18 Å) and chloro-substituent with Asp967 (2.73 Å) (Fig. 8 A_2, B_2 & C_2). Hence, superposition with OV5 reveals that the core scaffold of compound **5t** occupies a comparable region of the active site, reinforcing the notion that it exploits key pharmacophoric elements required for effective JAK3 inhibition.

2.3.2. Molecular dynamics simulation

The stability of the most active compound **5t** along with the corresponding native ligands, co-crystallized with the active sites of VEGFR2, FGFR1 and JAK3, were assessed through 200 ns molecular dynamics (MD) simulations.

2.3.2.1. Molecular dynamics simulation of compound 5t inside VEGFR2 active site. A 200 ns molecular dynamics (MD) simulation was performed in an explicit solvent environment to investigate the dynamic behavior of VEGFR2 in complex with compound **5t** and the reference inhibitor sunitinib. To evaluate the stability and robustness of the ligand–protein complexes, structural integrity was assessed through analyses of root mean square deviation (RMSD) and root mean square fluctuation (RMSF). The backbone RMSD analysis (C*α* atoms) demonstrated that both VEGFR-sunitinib and VEGFR-**5t** complexes remained stable throughout the 200 ns simulation, exhibiting fluctuations within the acceptable 3.0 Å threshold. Specifically, RMSD values ranged from 1.00 to 2.60 Å for the sunitinib complex and 1.30 - 2.90 Å for the **5t** complex, indicating a high degree of conformational stability for both systems. Ligand RMSD analysis revealed comparable dynamic behavior between the two compounds. Sunitinib displayed fluctuations ranging from 0.80 to 4.50 Å, while compound **5t** exhibited a similar behavior, fluctuating between 0.60 and 4.80 Å following initial equilibration, with occasional higher-fluctuation movements (Fig. 9: A_1, A_2). Additionally, RMSF analysis of VEGFR residues revealed well-maintained secondary structural elements, with α-helical regions remaining particularly stable, while higher flexibility was observed in loop regions. Active-site residues involved in ligand binding were highlighted along the X-axis. Both ligands consistently interacted with a conserved set of 15 key residues within the VEGFR active site namely: Lys838, Leu840, Val848, Glu850, Ala866, Val899, Glu917, Phe918, Cys919, Lys920, Phe921, Asn923, Thr926, Leu1035, and Phe1047, supporting a conserved binding mode for sunitinib and compound 5t (Fig. 9 B_1 & B_2). Fig. 9C and D panels present two-dimensional interaction diagrams, contact maps, and interaction histograms derived from the MD trajectories. Consistent with the docking results, both ligands formed two stable hydrogen bonds with Glu917 and Cys919 within the hinge region of the ATP-binding site. These interactions exhibited high persistence, with interaction fractions

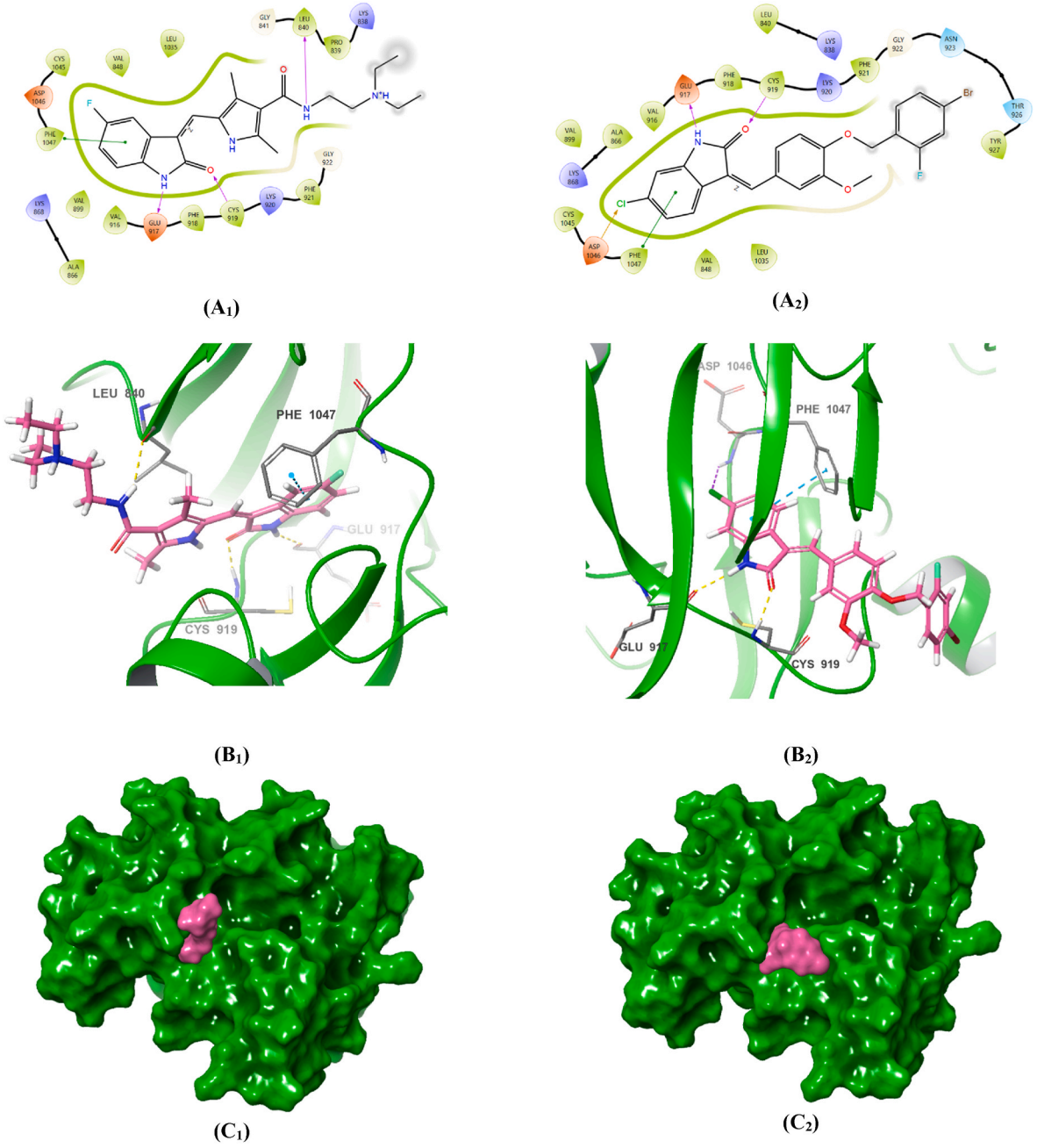


Fig. 6. Binding conformations of compound **5t** along with the native ligand sunitinib within the active site of the VEGFR enzyme. **($A_{1,2}$)** Two-dimensional schematic depicting key molecular interactions between compounds **5t** and sunitinib inside the VEGFR active site. **($B_{1,2}$)** Three-dimensional representation illustrating the spatial orientations of compounds **5t** and sunitinib (rendered in pink stick format) within the VEGFR binding pocket. **($C_{1,2}$)** Surface visualization of the VEGFR protein (depicted in green), demonstrating the surface-bound conformation of compounds **5t** and sunitinib using a green space-filling model.

of 99% for both residues in the sunitinib complex, and 97% and 96% for Glu917 and Cys919, respectively, in the **5t** complex. In addition, sunitinib formed a prominent water-mediated hydrogen bond with Asn923 (55%) and a notable intramolecular hydrogen bond between its protonated terminal amine and carboxamide carbonyl oxygen (57%). In contrast, compound **5t** exhibited a water-bridged hydrogen bond with Glu850 (30%) and a substantial π–π^* stacking interaction with the key hinge-region residue Phe1047 (32%). Collectively, these results demonstrate that both sunitinib and compound **5t** maintain stable binding conformations throughout the MD simulation, supporting favorable binding adaptability and sustained intermolecular interactions within the VEGFR active site. These findings further substantiate the potential of compound **5t** as a promising VEGFR inhibitor.

2.3.2.2. Molecular dynamics simulation of compound 5t inside FGFR active site. The Cα backbone RMSD analysis revealed distinct dynamic behaviors for the dovitinib-FGFR1 and **5t**-FGFR1 complexes during the MD simulation. For the dovitinib reference complex, RMSD values remained stable within 1.40 - 3.30 Å throughout the simulation. In contrast, the **5t**-FGFR1 complex exhibited RMSD values ranging from 1.50 to 3.50 Å during the first 100 ns, followed by a sudden increase from 3.50 to 4.10 Å toward the end of the simulation, exceeding the generally accepted stability threshold. Ligand RMSD analysis showed that dovitinib fluctuated within a range of 0.40–3.30 Å, exhibiting relatively high conformational flexibility. Similarly, compound 5t displayed an elevated fluctuation profile, with RMSD values increasing from 0.80 to 4.90 Å over the course of the simulation (Fig. 10 A_1 & A_2). Consistent

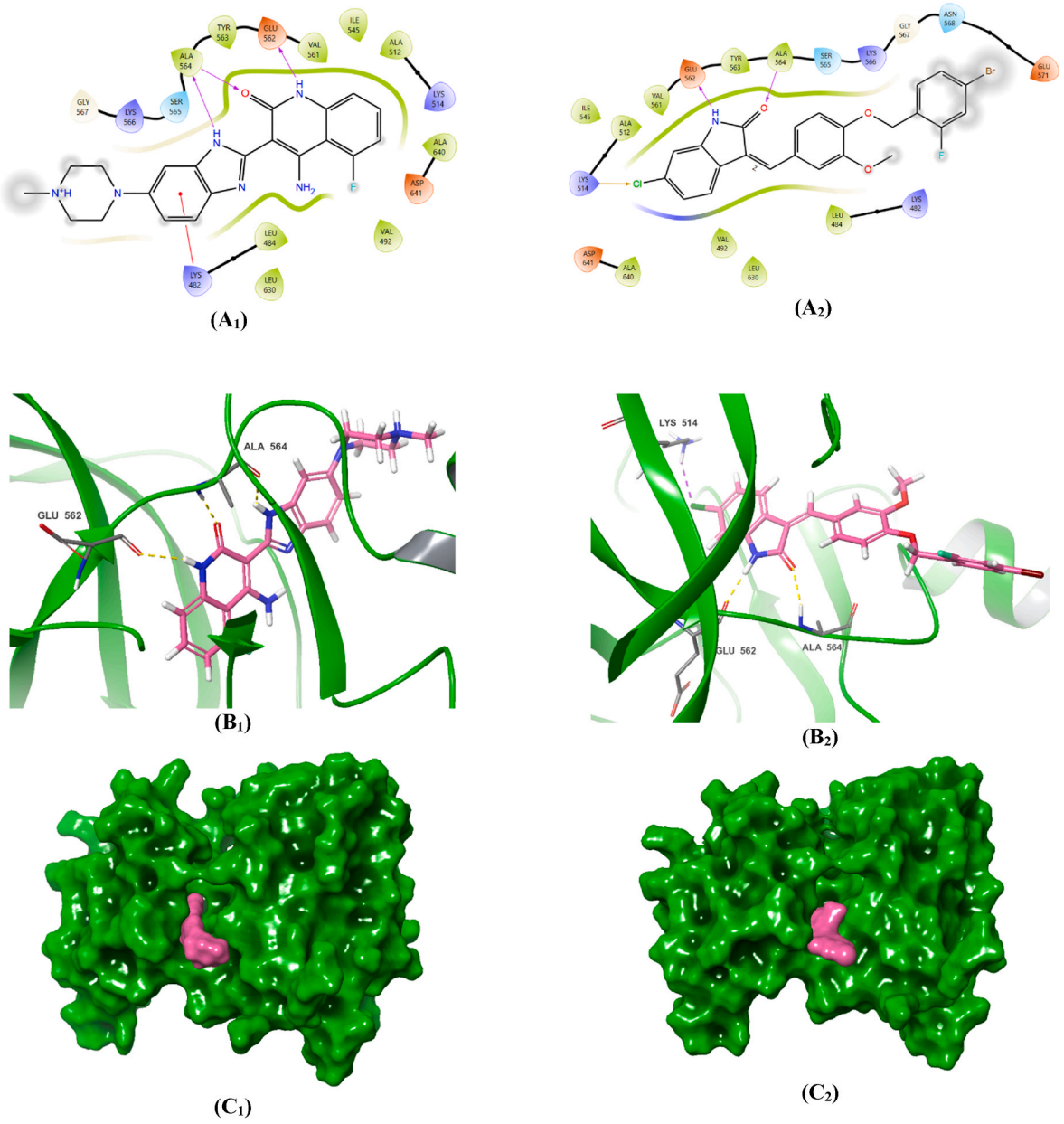


Fig. 7. Binding conformations of compound **5t** along with the native ligand dovitinib within the active site of the FGFR1 enzyme. **($A_{1,2}$)** Two-dimensional schematic depicting key molecular interactions between compounds **5t** and dovitinib inside the FGFR1 active site. **($B_{1,2}$)** Three-dimensional representation illustrating the spatial orientations of compounds **5t** and dovitinib (rendered in pink stick format) within the FGFR1 binding pocket. **($C_{1,2}$)** Surface visualization of the FGFR1 protein (depicted in green), demonstrating the surface-bound conformation of compounds **5t** and dovitinib using a green space-filling model.

with these observations, RMSF analysis of FGFR1 residues demonstrated that both ligands-maintained contacts with a conserved set of 14 key residues throughout the 200 ns simulation, namely Lys482, Leu484, Val492, Ala512, Ile545, Val561, Glu562, Tyr563, Ala564, Lys566, Asn568, Glu571, Leu630, and Ala640. This shared interaction pattern suggests a similar binding mode for dovitinib and compound **5t** within the FGFR1 active site (Fig. 10 B_1 & B_2). Two-dimensional ligand-protein interaction diagrams and contact histograms further revealed that both ligands formed persistent hydrogen bonds with Glu562 (interaction fractions of 97% for dovitinib and 99% for **5t**) and Ala564 (154% for dovitinib and 96% for **5t**). Additionally, dovitinib exhibited two prominent intramolecular hydrogen bonds involving the benzimidazole nitrogen atoms and the 2-quinolone carbonyl oxygen and amino group of 2-quinolone scaffold, with interaction frequencies of 43% and 71%, respectively. In contrast, compound **5t** formed an additional hydrophobic interaction with Leu630, exhibiting an interaction fraction of 60%. Overall, these findings demonstrate that compound **5t** is capable of forming and maintaining interactions within the FGFR1 active site throughout the MD simulation in a manner comparable to the reference inhibitor dovitinib, despite increased structural fluctuations. These results support the potential of compound **5t** as an FGFR1-binding agent and warrant further experimental evaluation to confirm its predicted inhibitory activity.

2.3.2.3. Molecular dynamics simulation of compound 5t inside JAK3 active site. The C*α* backbone RMSD analysis demonstrated that both the OV5-JAK3 and **5t**-JAK3 complexes remained structurally stable throughout the MD simulation. RMSD values were maintained within 2.70 Å for the OV5-JAK3 complex and 2.40 Å for the **5t**-JAK3 complex, both initiating from approximately 1.30 Å, and remaining well within acceptable

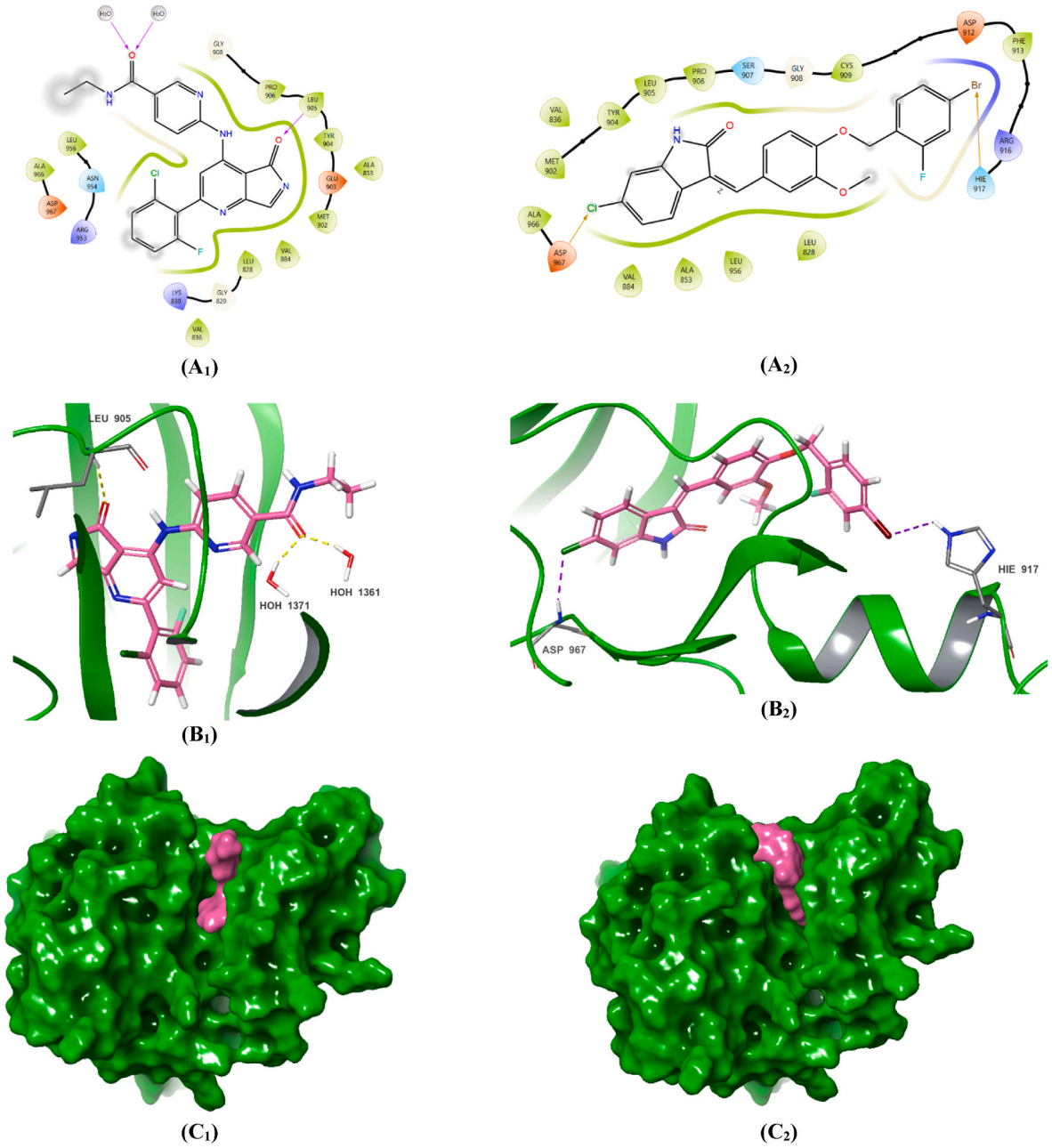


Fig. 8. Binding conformations of compound **5t** along with the native ligand **OV5** within the active site of the JAK3 enzyme. **($A_{1,2}$)** Two-dimensional schematic depicting key molecular interactions between compounds **5t** and OV5 inside the JAK3 active site. **($B_{1,2}$)** Three-dimensional representation illustrating the spatial orientations of compounds **5t** and OV5 (rendered in pink stick format) within the JAK3 binding pocket. **($C_{1,2}$)** Surface visualization of the JAK3 protein (depicted in green), demonstrating the surface-bound conformation of compounds **5t** and OV5 using a green space-filling model.

stability limit. In addition, ligand RMSD analysis revealed that the OV5 reference ligand stabilized at approximately 4.50 Å, starting from about 1.00 Å, whereas compound **5t** exhibited higher flexibility, with RMSD values increasing from 1.60 Å to 5.80 Å over the course of the simulation (Fig. 11 A_1 & A_2). Cooperatively, these findings indicate that both OV5-JAK3 and 5t-JAK3 complexes maintained satisfactory conformational stability throughout the simulation period. RMSF analysis further demonstrated that both ligands interacted with a conserved set of 14 key residues during the dynamic simulation, namely Ser826, Gln827, Leu828, Val836, Ala853, Tyr904, Leu905, Pro906, Cys909, Arg911, Asp912, Arg916, Leu956, and Asp967. This shared interaction pattern supports a similar binding mode for compound 5t and the native ligand within the JAK3 active site (Fig. 11 B_1 & B_2). The ligand-protein contact histograms revealed that the OV5 ligand formed two predominant interactions: a persistent hydrogen bond with Leu905 (99%) and a hydrophobic interaction with Leu956 (55%). Additionally, OV5 exhibited a stable intramolecular hydrogen bond between its secondary amine and the 2-pyrrolone carbonyl oxygen (79%). In contrast, compound **5t** displayed a more diverse interaction profile, including water-mediated hydrogen bonds with Asp912 (93%) and Cys909 (65%), a π–cation interaction with Arg916 (31%), and hydrophobic contacts with Leu828 (53%), Ala853 (50%), and Leu956 (40%). Overall, these results confirm the ability of compound **5t** to maintain stable and productive interactions within the JAK3 active site throughout the MD simulation. The observed binding behavior supports its potential as a JAK3 inhibitor and warrants further experimental evaluation to validate its predicted inhibition activity.

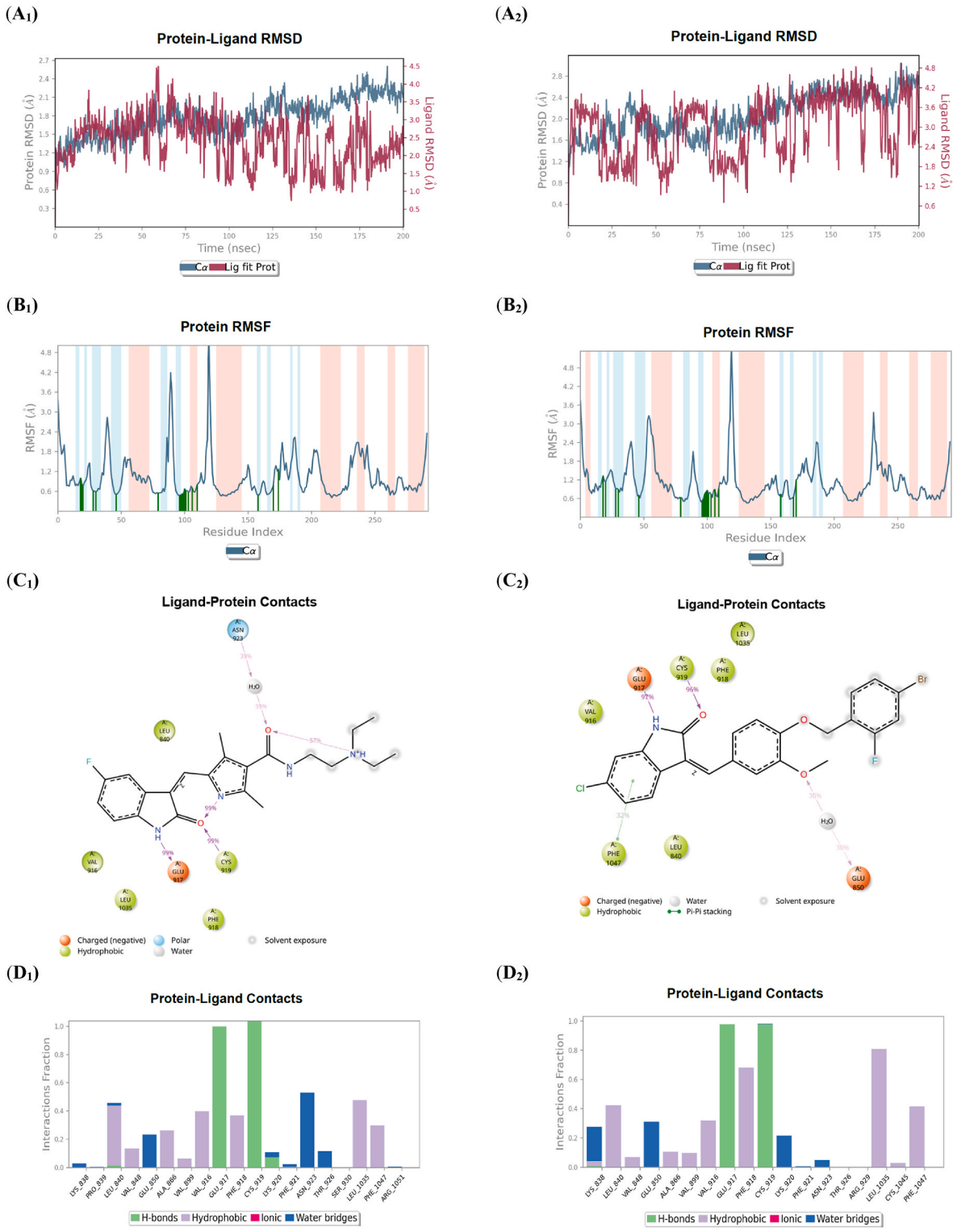


Fig. 9. Molecular dynamics (MD) simulation analysis of the investigated compound **5t** and the native ligand sunitinib bound to the VEGFR active site. **($A_{1,2}$)** Root Mean Square Deviation (RMSD) plots for the VEGFR protein (gray) and ligands sunitinib and **5t** (red), reflecting the structural stability of the formed complex over the course of the simulation. **($B_{1,2}$)** Root Mean Square Fluctuation (RMSF) plots of VEGFR residues, indicating regions of local flexibility in response to ligand binding. **($C_{1,2}$)** Two-dimensional interaction maps illustrating key ligand-protein contacts maintained throughout the simulation. **($D_{1,2}$)** Histograms representing the frequency and types of ligand-protein interactions, providing insight into the stability and persistence of binding over time.

2.4. DFT and quantum chemical analysis

To gain deeper insight into the electronic factors that govern the antileukemic activity of the oxindole series **5a–5t**, quantum chemical calculations were carried out with Gaussian at the B3LYP, HF, and M06-2X levels using the 6-31++G(d,p) basis set. On the basis of frontier molecular orbital (FMO) energies, we derived a set of global reactivity descriptors for each compound, including EHOMO, ELUMO, the HOMO–LUMO energy gap (ΔE), ionization potential (I), electron affinity (A), chemical hardness (η), chemical potential (μ), electronegativity (χ),

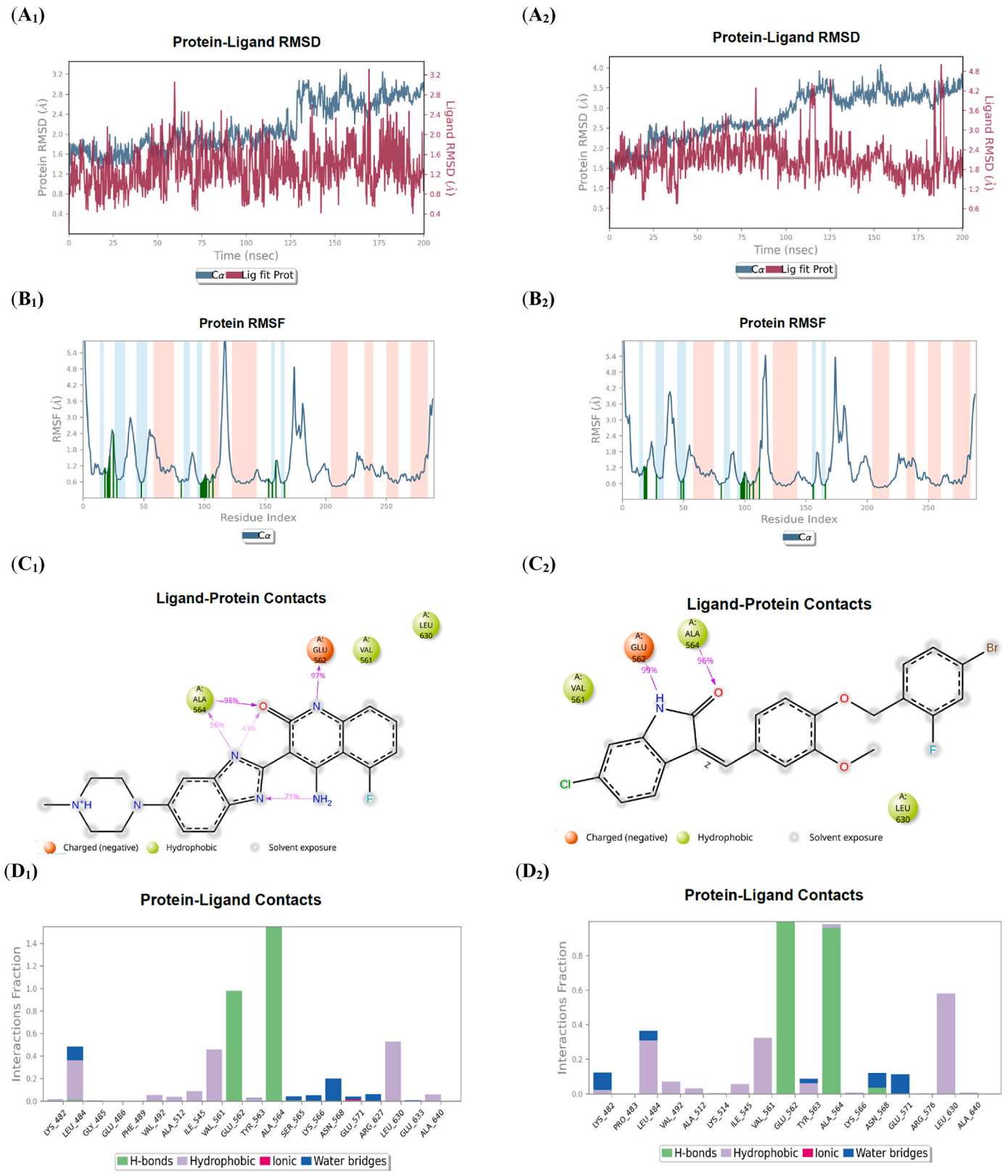


Fig. 10. Molecular dynamics (MD) simulation analysis of the investigated compound **5t** and the native ligand dovitinib bound to the FGFR1 active site. **($A_{1,2}$)** Root Mean Square Deviation (RMSD) plots for the FGFR1 protein (gray) and ligands dovitinib and **5t** (red), reflecting the structural stability of the formed complex over the course of the simulation. **($B_{1,2}$)** Root Mean Square Fluctuation (RMSF) plots of FGFR1 residues, indicating regions of local flexibility in response to ligand binding. **($C_{1,2}$)** Two-dimensional interaction maps illustrating key ligand-protein contacts maintained throughout the simulation. **($D_{1,2}$)** Histograms representing the frequency and types of ligand-protein interactions, providing insight into the stability and persistence of binding over time.

electrophilicity index (ω), nucleophilicity index (ε), and dipole moment. The complete data set is summarized in Table S5, while the optimized geometries, HOMO/LUMO distributions and electrostatic potential (ESP) maps are depicted in Fig. S1 [31,32]. EHOMO is associated with the electron-donating ability of a molecule, whereas ELUMO and the corresponding ΔE = ELUMO − EHOMO describe its electron-accepting capacity and overall electronic stability. Across the present library, the calculated FMOs consistently reflect the dominant electronic role of the oxindole motif: the oxindole–vinyl–aryl conjugated backbone supports delocalization of the frontier orbitals and enables a balanced donor–acceptor character that is compatible with charge-transfer and polarization effects in biological environments. Within the oxindole

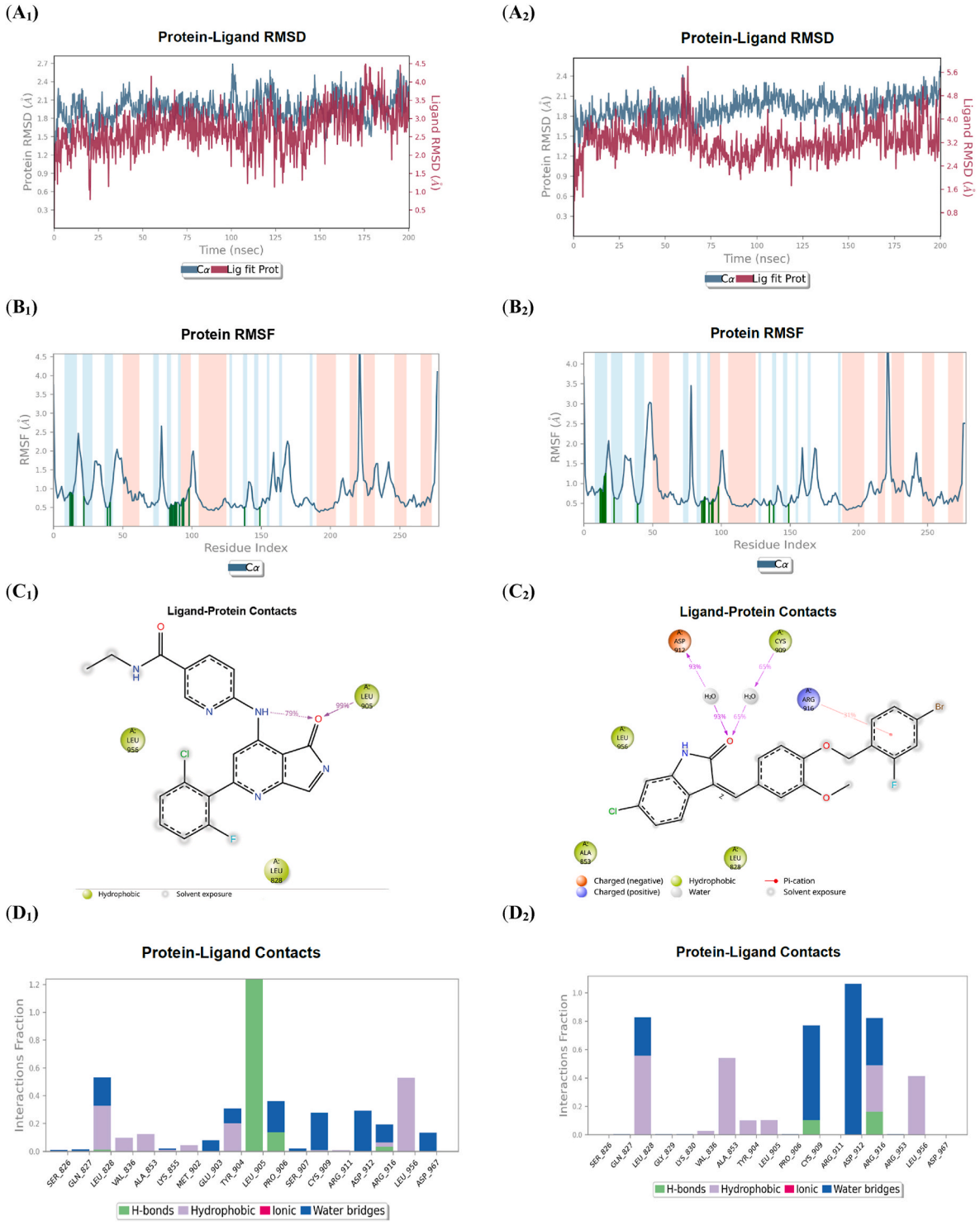


Fig. 11. Molecular dynamics (MD) simulation analysis of the investigated compound **5t** and the native ligand OV5 bound to the JAK3 active site. **($A_{1,2}$)** Root Mean Square Deviation (RMSD) plots for the JAK3 protein (gray) and ligands OV5 and **5t** (red), reflecting the structural stability of the formed complex over the course of the simulation. **($B_{1,2}$)** Root Mean Square Fluctuation (RMSF) plots of JAK3 residues, indicating regions of local flexibility in response to ligand binding. **($C_{1,2}$)** Two-dimensional interaction maps illustrating key ligand-protein contacts maintained throughout the simulation. **($D_{1,2}$)** Histograms representing the frequency and types of ligand-protein interactions, providing insight into the stability and persistence of binding over time.

series, the B3LYP HOMO–LUMO gaps fall within a relatively narrow window (ca. 3.43–3.58 eV), reflecting a favorable balance between kinetic stability and chemical responsiveness. Importantly, this conserved ΔE range indicates that the shared oxindole-centered π-system provides a common electronic platform across the series, while peripheral substitution primarily modulates the extent of polarization and the spatial distribution of the FMOs rather than redefining the fundamental reactivity pattern [31,33].

The calculated hardness values (η ≈ 1.71–1.79 eV at the B3LYP level) show that the oxindole hybrids are not overly soft: they retain sufficient intrinsic stability while remaining reactive enough to participate in polar and charge-transfer processes within a protein binding site. In parallel, the electrophilicity index (ω) spans approximately 4.53–5.15, consistent with an electrophilic scaffold that can accept electron density during binding and stabilization by polar residues. Taken together, the hardness/electrophilicity profiles support the view that the antileukemic potential is rooted in the oxindole pharmacophore, which combines a stable heteroaromatic core with a conjugated framework capable of adaptive polarization; substituent changes mainly adjust the magnitude of these effects and may tune complementarity to a given binding pocket without altering the central role of the oxindole unit.

At the HF level, which provides a complementary description of the gas-phase electronic structure, the same global descriptors support a polar, moderately electrophilic scaffold capable of establishing hydrogen-bonding and electrostatic interactions with charged or polar residues in kinase active sites. In this regard, the conjugated oxindole–vinyl–aryl framework, together with the carbonyl, sulfonamide and heteroatom functionalities, promotes HOMO delocalization over the π-system, while the LUMO is consistently shifted towards the more electron-deficient fragments (Fig. 12) This recurrent "push-pull" organization anchored by the oxindole ring provides a coherent electronic basis for productive charge redistribution during ligand-target recognition, while peripheral groups primarily fine-tune the directionality and strength of this polarization [34].

The potent derivative **5t** exhibited EHOMO = −7.76 eV and ELUMO = −1.84 eV, corresponding to an energy gap of 5.92 eV and a hardness of 2.96 eV (Table 7). Its electronegativity (χ ≈ 4.80 eV), electrophilicity index (ω ≈ 3.90 eV) and sizable dipole moment (~4.5 D) further support a polar, moderately electrophilic scaffold capable of establishing hydrogen-bonding and electrostatic interactions with charged or polar residues in kinase active sites.

The FMO and ESP analyses (Fig. S1) further reinforce this interpretation. Across representative structures, the oxindole carbonyl and adjacent heteroatoms generate pronounced electrostatic features that are well suited for hydrogen bonding and dipolar contacts, while the extended π-system enables delocalization and electronic communication between the heteroaromatic core and the aryl/sulfonamide regions. Thus, the electronic descriptors collectively support that the observed antileukemic behaviour of this compound set is primarily dictated by the presence of the oxindole scaffold and its conjugated architecture, with substitution patterns serving mainly to modulate electronic polarization, local electrostatic potential, and steric/lipophilic complementarity rather than acting as the principal origin of activity [31].

Overall, the DFT data provide a coherent electronic rationale for the biological relevance of the oxindole series as a whole. The combination of (i) frontier orbitals delocalized over the oxindole-centered conjugated core, (ii) moderate HOMO–LUMO gaps and hardness values compatible with controlled reactivity, and (iii) electrophilicity/dipole characteristics indicative of efficient polar recognition, supports an enhanced capacity of these molecules to engage in charge-transfer and noncovalent

Table 7
Electronic properties of compound **5t** at the B3LYP, HF, and M06-2X Levels.

Property	B3LYP/6-31++G(d,p)	HF/6-31++G(d,p)	M06-2X/6-31++G(d,p)
E_{HOMO} (eV)	−5.9294	−8.1099	−7.1931
E_{LUMO} (eV)	−2.4695	0.9192	−1.6126
Ionization potential, I (eV)	5.9294	8.1099	7.1931
Electron affinity, A (eV)	2.4695	−0.9192	1.6126
Energy gap, ΔE (eV)	3.4600	9.0291	5.5806
Chemical hardness, η (eV)	1.7300	4.5145	2.7903
Chemical potential, μ (eV)	0.5780	0.2215	0.3584
Electronegativity, χ (eV)	4.1994	3.5953	4.4028
Proton affinity, PA (eV)	−4.1994	−3.5953	−4.4028
Electrophilicity index, ω (eV)	5.0969	1.4316	3.4737
Nucleophilicity index, ε (eV)	0.1962	0.6985	0.2879
Dipole moment (D)	1.995	3.5042	1.5288
Total energy (a.u.)	−116957.0856	−116696.3928	−116944.1543

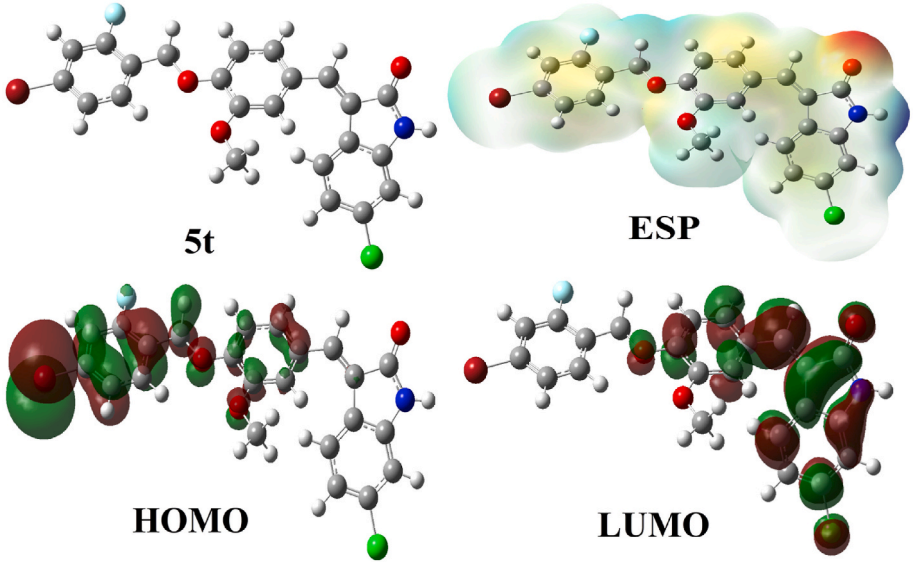


Fig. 12. Representations of optimize structure, HOMO, LUMO, and ESP of compound **5t.**

interactions with kinase targets and related biomacromolecules. In this context, the DFT outcomes emphasize the oxindole ring as the key structural driver underlying the activity of the library, while the substituents mainly provide incremental tuning of the electronic landscape.

2.5. ADME results

In silico ADME profiling revealed that **5t** was the best candidate for development since it had an optimal molecular size and polarity (MW = 489, PSA = 62 Å^2, HBD/HBA = 1/4) and a highly favorable anticipated absorption profile. **5t** had a high lipophilicity (QPlogPo/w = 5.9), but it also had great potential membrane permeability, as seen by high Caco-2 and MDCK values, translating into a predicted 100% human oral absorption (Table 8). Compound **5t** has a well-balanced lipophilic profile that helps it diffuse through membranes without losing solubility. The predicted aqueous solubility values (QPlogS, −7.3; CIQPlogS = −8.9 for **5t**) suggest that it is soluble enough compared to the other compounds in the series, indicating that its substitution pattern partially mitigates excessive hydrophobicity while preserving permeability. The distribution-related characteristics were good for a non-CNS oncology drug. The anticipated brain penetration was minimal (QPlogBB = −0.2) and the albumin-binding tendency was moderate to high (QPlogKhsa = 1.0). This could lead to systemic exposure while lowering off-target CNS effects. The estimated metabolic liability was modest (metab = 3), consistent with its molecular complexity. The predicted hERG inhibition parameter (QPlogHERG = −6.1) shows that it may have a lower risk of causing cardiotoxicity than other members of the series. Overall, compound **5t** stands up as a strong candidate since it has moderate lipophilicity, good solubility, and higher cellular permeability than other compounds. These characteristics endorse its designation as a viable scaffold for subsequent *in vivo* pharmacokinetic and pharmacodynamic assessment.

3. Conclusion and future perspectives

In conclusion, a series of oxindole-based derivatives (**5a-t**) was successfully designed, synthesized, and evaluated as potential anti-leukemic agents. *In vitro* screening through the NCI-DTP identified compound **5t** as the most potent analogue, exhibiting broad anti-proliferative activity across the NCI-60 panel with GI_{50} (MG-MID) values ranging from 9.05 to 45.24 μM and exhibiting pronounced efficacy against leukemia cell lines. Structure activity relationship analysis revealed that a combination of a 6-chloro oxindole core, a 2-fluoro-4-bromobenzyl substituent, and a vanillin-derived aromatic linker was critical for enhanced potency and selectivity. Compound **5t** demonstrated superior cytotoxicity against CCRF-CEM cells (IC_{50} = 2.92 μM) compared to ibrutinib, while showing markedly improved selectivity toward leukemic cells over normal fibroblast cells (BJ and MRC-5; SI > 17). Mechanistic studies indicated that **5t** functions as a multi-kinase inhibitor, effectively targeting JAK3, VEGFR2, and FGFR1 and induces dose-dependent S- and G2/M-phase cell cycle arrest. Molecular docking coupled with 200 ns molecular dynamics simulations confirmed stable binding of **5t** within the active sites of JAK3 and VEGFR2. Furthermore, *In silico* ADME and DFT analyses supported the compound's favorable drug-like and electronic properties. Collectively, these findings identify compound **5t** as a viable candidate for further preclinical evaluation as multi-kinase inhibitors with potent and selective anti-leukemia activity, while the proposed pharmacological, pharmacokinetic, and *in vivo* studies will be essential to establish its translational potential in acute lymphoblastic leukemia.

Table 8
Key physicochemical and ADME properties of compound **5t**.

Property	5t	Reference range	Property	5t	Reference range
Molecular weight (Da)	489	130–725	CIQPlogS	−8.9	−6.5-0.5
Dipole moment (D)	1.4	1.0–12.5	QPlogHERG	−6.1	*
SASA (Å^2)	696	300–1000	QPPCaco (nm/sec)	1554	**
FOSA (Å^2)	120	0–750	QPlogBB	−0.2	−3.0-1.2
WPSA (Å^2)	187	0–175	QPPMDCK (nm/sec)	8454	**
Volume (Å^3)	1247	500–2000	QPlogKhsa	1.0	−1.5-1.5
HBD	1	0–6	No. of metabolic sites	3	1–8
HBA	4	2.0-20.0	Human oral absorption (%)	100	-
QPlogPo/w	5.9	−2.0–6.5	Lipinski's rule violations	1	Maximum is 4
QPlogPw	8.2	4.0–45.0	Jorgensen's rule violations	1	Maximum is 3
QPlogS	−7.3	−6.5-0.5	PSA	62	7-200

4. Materials and methods

4.1. Chemistry

All chemicals and organic solvents utilized to synthesize the desired compounds are of commercial grade and purchased from Alfa Aesar, Sigma Aldrich, Merck, and El-gomhoria companies for pharmaceutical and used without further purification. Reaction progress was monitored using pre-coated TLC plates (Kiesslgel 60 F_{254}, Merck), detecting spots was done *via* UV lamp at a wavelength of 254 nm. Melting points were measured on Stuart Electro-Thermal apparatus and recorded without correction. ^{1}H NMR was carried out on a JOEL JNM-ECA400 (^{1}HNMR: 400 MHz, ^{13}C NMR: 100 MHz) spectrophotometer at Zagazig University, Egypt. Chemical shifts were recorded in parts per million (ppm) compared to standard TMS using deuterated DMSO (δ: 2.5 ppm) as a solvent and the coupling constant (J) is measured in hertz (Hz). Multiplicity was designated as: s, singlet; d, doublet; t, triplet; q, quartet; p, pentet; dd, doublet of doublet; and m for multiplet. Elemental Analysis were performed at the regional center for mycology and biotechnology, Al-Azhar University, Nasr city, Cairo, Egypt.

4.1.1. General procedure for the synthesis of compounds 3a-e

A mixture of the appropriate alkyl halide (**1a-e**, 1 mmol), *p*-hydroxy benzaldehyde **2a** (1 mmol, 122 mg) or vanillin **2b** (1 mmol, 152 mg), and potassium carbonate (1 mmol, 135 mg) was heated to reflux in acetonitrile (20 mL) for 24 h. The reaction progress was monitored *via* TLC, then the reaction mixture was concentrated under reduced pressure and the remaining mixture was extracted using ethyl acetate (3 X 30 mL (and washed with water (3 X 30 mL). The organic layer was collected and dried over anhydrous sodium sulfate. The solvent was filtered off to yield compounds **3a-e** that were used for the following steps without additional purification.

4.1.1.1. 4-((4-Bromo-2-fluorobenzyl)oxy)benzaldehyde (3a). Off-white solid; 65% yield (163 mg); mp: 75-75°C, reported mp: 73-77°C; R_F = 0.34 (pet.ether: EtOAc, 3:1) [35].

4.1.1.2. 4-((4-Bromobenzyl)oxy)benzaldehyde (3b). White solid; 77% yield (165.5 mg); mp: 96-99°C, reported mp: 95-97°C; R_F = 0.25 (pet. ether: EtOAc, 3:1) [36].

4.1.1.3. 4-((2-Fluorobenzyl)oxy)benzaldehyde (3c). Yellow solid; 79% yield (165 mg); mp: 57-55.5°C, reported mp: 55-59°C; R_F = 0.30 (pet. ether: EtOAc, 3:1) [37].

4.1.1.4. 4-((4-Bromo-2-fluorobenzyl)oxy)-3-methoxybenzaldehyde (3d).

Yellow solid; 50% yield (176 mg); mp: 75-77°C; $R_F = 0.32$ (pet. ether: EtOAc, 3:1)

4.1.1.5. 4-((4-Bromobenzyl)oxy)-3-methoxybenzaldehyde (3e). Yellow solid; 55% yield (190 mg); mp: 55-55°C, reported mp: 57-90°C; $R_F = 0.33$ (pet. ether: EtOAc, 3:1) [38].

4.1.2. General procedure for the synthesis of compounds 5a-t

Indolin-2-ones (**4a-d**, 1 mmol) were added to a solution of appropriate alkylated vanillin or alkylated *p*-hydroxybenzaldehyde derivatives (**3a-e**, 1 mmol) in EtOH (10 mL). A catalytic amount of piperidine was added as base, and the reaction mixture was heated at reflux for 3-6 h. Reaction progress was monitored using TLC. After completion, the reaction mixture is allowed to cool. The formed precipitate was filtered off and washed with EtOH to yield compounds **5a-t**.

4.1.3. 3-(4-((2-Fluorobenzyl)oxy)benzylidene)indolin-2-one (5a)

Yellow powder; 77% yield (134 mg); mp: 165-171°C, $R_F = 0.39$ (pet. ether: EtOAc, 1:1). ^{1}H NMR (400 MHz, DMSO-d_6) δ: 10.57 (s, 1H, NH), 7.74 (dd, $J = 7.7$ Hz, 1H, Ar-H), 7.71 (s, 1H, C=CH), 7.69–7.60 (m, 2H, Ar-H), 7.55 (d, 1H, Ar-H), 7.45 (d, $J = 7.4$ Hz, 1H, Ar-H), 7.27 (dd, $J = 5.6$ Hz, 2H, Ar-H), 7.23 (d, $J = 7.9$ Hz, 1H, Ar-H), 7.20 (t, 1H, Ar-H),7.19 – 7.07 (m, 1H, Ar-H), 7.02 – 6.79 (m, 2H, Ar-H), 5.24 (s, 2H, CH_2). ^{13}C NMR (100 MHz, DMSO-d_6) δ: 165.55, 159.43, 142.70, 140.29, 135.56, 134.39, 131.51, 130.59, 130.55, 129.74, 127.05, 125.52, 124.60, 124.56, 124.25, 121.12, 121.05, 115.55, 115.34, 114.96, 114.42, 63.51. Anal. Calcd. For $C_{22}H_{16}FNO_2$ (345.37) C, 76.51; H, 4.67; N, 4.06. found: C, 76.52; H, 4.65; N, 4.07.

4.1.4. 5-Fluoro-3-(4-((2-fluorobenzyl)oxy)benzylidene)indolin-2-one (5b)

Yellow powder; 51% yield (125 mg); mp: 155-190°C, $R_F = 0.42$ (pet. ether: EtOAc, 1:1). ^{1}H NMR (400 MHz, DMSO-d_6) δ 10.60 (s, 1H, NH), 5.74–5.46 (m, 1H, Ar-H), 7.75 (dd, $J = 5.3$ Hz, 2H, Ar-H), 7.69 (s, 1H, C=CH), 7.56 (m, 1H, Ar-H), 7.45 (dd, $J = 7.0$ Hz, 1H, Ar-H), 7.40 – 7.13 (m, 4H, Ar-H), 7.12–6.96 (m, 1H, Ar-H), 6.52 (dd, $J = 4.5$ Hz, 1H, Ar-H), 5.24 (s, 2H, CH_2). ^{13}C NMR (100 MHz, DMSO-d_6) δ: 165.55, 167.40, 160.37, 159.71, 159.24, 139.02, 136.46, 134.69, 131.61, 130.59, 130.55, 130.63, 130.55, 127.14, 126.62, 124.55, 124.55, 115.54, 115.33, 115.05, 114.51, 63.75. Anal. Calcd. For $C_{22}H_{15}F_2NO_2$ (363.36) C, 72.72; H, 4.16; N, 3.55. found: C, 72.73; H, 4.17; N, 3.56.

4.1.5. 5-Chloro-3-(4-((2-fluorobenzyl)oxy)benzylidene)indolin-2-one (5c)

Yellow powder; 76% yield (110 mg); mp: 154-156°C, $R_F = 0.35$ (pet. ether: EtOAc, 1:1). ^{1}H NMR (400 MHz, DMSO-d_6) δ 10.64 (s, 1H, NH), 5.67 – 5.47 (m, 2H, Ar-H), 7.94 – 7.75 (m, 1H, Ar-H), 7.76 – 7.65 (s, 1H, C=CH), 7.65 – 7.53 (m, 1H, Ar-H), 7.44 (dd, $J = 5.1$ Hz, 1H, Ar-H), 7.37 – 7.19 (m, 4H, Ar-H), 7.16 (d, $J = 5.9$ Hz, 1H, Ar-H), 6.59 (d, $J = 5.3$ Hz, 1H, Ar-H), 5.25 (s, 2H, CH_2). ^{13}C NMR (100 MHz, DMSO-d_6) δ 160.51, 159.53, 135.94, 134.55, 131.69, 130.97, 130.66, 130.09, 127.34, 127.23, 126.65, 125.39, 125.02, 124.67, 124.63, 123.20, 115.62, 115.41, 115.15, 115.15, 114.60, 63.57. Anal. Calcd. For $C_{22}H_{15}ClFNO_2$ (379.52) C, 69.57; H, 3.95; N, 3.69. found: C, 69.55; H, 3.99; N, 3.70.

4.1.6. 6-Chloro-3-(4-((2-fluorobenzyl)oxy)benzylidene)indolin-2-one (5d)

Yellow powder; 65% yield (117 mg); mp: 205-210°C, $R_F = 0.41$ (pet. ether: EtOAc, 1:1). ^{1}H NMR (400 MHz, DMSO-d_6) δ: 10.73 (s, 1H, NH), 5.47 (d, $J = 5.9$ Hz, 1H, Ar-H), 7.73 (dd, 2H, Ar-H), 7.67–7.54 (s, 1H, C=CH), 7.49 – 7.40 (m, 2H, Ar-H), 7.35 – 7.23 (m, 2H, Ar-H), 7.17 (dd, $J = 5.5$ Hz, 2H, Ar-H), 7.11 – 6.50 (m, 2H, Ar-H), 5.23 (s, 2H, CH_2). ^{13}C NMR (100 MHz, DMSO-d_6) δ: 165.52, 159.62, 144.00, 141.35, 136.77, 134.55, 133.64, 131.65, 130.55, 130.55, 127.19, 126.77, 124.64, 124.56, 120.79, 120.70, 120.06, 115.55, 115.34, 115.03, 114.49, 63.53. Anal. Calcd. For $C_{22}H_{15}ClFNO_2$ (379.52) C, 69.57; H, 3.95; N, 3.69. found: C, 69.55; H, 3.99; N, 3.70.

4.1.7. 3-(4-((4-Bromobenzyl)oxy)benzylidene)indolin-2-one (5e)

Yellow powder; 55% yield (100 mg); mp: 215-222°C, $R_F = 0.24$ (pet. ether: EtOAc, 1:1). ^{1}H NMR (400 MHz, DMSO-d_6) δ 10.56 (s, 1H, NH), 7.73 (d, $J = 7.7$ Hz, 1H, Ar-H), 7.69 (s, 1H, C=CH), 7.63 (d, $J = 10.0$ Hz, 2H, Ar-H), 7.61–7.55 (m, 2H, Ar-H), 7.45 (d, $J = 5.3$ Hz, 2H, Ar-H), 7.22 (t, $J = 7.7$ Hz, 1H, Ar-H)), 7.16 (d, $J = 5.7$ Hz, 1H, Ar-H), 7.10 (d, $J = 5.5$ Hz, 1H, Ar-H), 7.04 – 6.77 (m, 2H, Ar-H), 5.19 (s, 2H, CH_2). ^{13}C NMR (100 MHz, DMSO-d_6) δ: 165.57, 159.40, 142.65, 136.67, 136.19, 135.55, 134.36, 131.50, 131.42, 129.93, 129.74, 127.29, 126.96, 125.77, 122.07, 121.12, 121.04, 120.90, 119.27, 115.05, 110.04, 65.60. Anal. Calcd. For $C_{22}H_{16}BrNO_2$ (406.25) C, 65.04; H, 3.97; N, 3.45; found C, 65.05; H, 3.95; N, 3.46.

4.1.8. 3-(4-((4-Bromobenzyl)oxy)benzylidene)-5-fluoroindolin-2-one (5f)

Yellow powder; 59% yield (122 mg); mp: 239-241°C, $R_F = 0.36$ (pet. ether: EtOAc, 1:1). ^{1}H NMR (400 MHz, DMSO-d_6) δ 10.55 (s, 1H, NH), 5.45 (d, $J = 5.5$ Hz, 1H, CH), 7.76 (s, 1H, C=CH) 7.66 – 7.57 (m, 3H, Ar-H), 7.44 (dd, $J = 5.3$ Hz, 2H, Ar-H), 7.34 (dd, $J = 9.4$ Hz, 1H, Ar-H), 7.25 – 6.95 (m, 3H, Ar-H), 6.52 (dd, $J = 5.5$ Hz, 1H, Ar-H), 5.19 (s, 2H, CH_2). ^{13}C NMR (100 MHz, DMSO-d_6) δ 169.34, 167.55, 160.53, 160.15, 135.90, 135.05, 136.61, 136.59, 135.16, 132.05, 131.59, 130.42, 130.41, 127.55, 127.02, 121.60, 116.55, 116.32, 115.67, 115.13, 107.05, 69.11. Anal. Calcd. For $C_{22}H_{15}BrFNO_2$ (424.27) C, 62.25; H, 3.56; N, 3.30 found C, 62.29; H, 3.57; N, 3.31.

4.1.9. 3-(4-((4-Bromobenzyl)oxy)benzylidene)-5-chloroindolin-2-one (5g)

Yellow powder; 65% yield (90 mg); mp: 225-230°C, $R_F = 0.3$ (pet. ether: EtOAc, 1:1). ^{1}H NMR (400 MHz, DMSO-d$_6$) δ 10.71 (s, 1H, NH), 5.49 (d, $J = 5.9$ Hz, 1H, CH), 7.55 (s, 1H, C=CH), 7.55–7.64 (m, 2H, Ar-H), 7.64–7.52 (m, 2H, Ar-H), 7.45 (dd, $J = 5.2$ Hz, 2H, Ar-H), 7.25 (dd, $J = 5.3$ Hz, 1H, Ar-H), 7.24 – 7.07 (m, 2H, Ar-H), 6.55 (dd, $J = 5.3$ Hz, 1H, Ar-H), 5.20 (s, 2H, CH_2). ^{13}C NMR (100 MHz, DMSO-d_6) δ 160.90, 139.35, 139.19, 135.34, 136.59, 135.24, 132.07, 131.90, 130.46, 130.43, 129.70, 127.76, 127.59, 127.01, 125.77, 123.57, 121.60, 119.51, 115.65, 115.15, 111.02, 69.11, 69.06. Anal. Calcd. For $C_{22}H_{15}BrClNO_2$ (440.72) C, 59.96; H, 3.43; N, 3.15 found C, 59.97; H, 3.44; N, 3.19.

4.1.10. 3-(4-((4-Bromobenzyl)oxy)benzylidene)-6-chloroindolin-2-one (5h)

Yellow powder; 65% yield (50 mg); mp: 247-250°C, $R_F = 0.35$ (pet. ether: EtOAc, 1:1). ^{1}H NMR (400 MHz, DMSO-d_6) δ 10.73 (s, 1H, NH), 5.46 (d, $J = 5.9$ Hz, 2H, Ar-H), 7.53 – 7.66 (s, 1H, C=CH), 7.61 (dd, $J = 5.5$ Hz, 3H, Ar-H), 7.44 (dd, $J = 5.5$ Hz, 2H, Ar-H), 7.23 – 7.06 (m, 2H, Ar-H), 7.06 – 6.79 (m, 2H, Ar-H), 5.17 (s, 2H, CH_2). ^{13}C NMR (100 MHz, DMSO-d_6) δ: 169.32, 160.09, 144.50, 135.30, 137.25, 136.62, 135.05, 134.12, 132.13, 131.91, 130.41, 127.15, 125.05, 123.76, 121.60, 121.26, 120.55, 115.65, 115.11, 110.46, 109.63, 69.11. Anal. Calcd. For $C_{22}H_{15}BrClNO_2$ (440.72) C, 59.96; H, 3.43; N, 3.15 found C, 59.97; H, 3.44; N, 3.19.

4.1.11. 3-(4-((4-bromo-2-fluorobenzyl) oxy) benzylidene) indolin-2-one (5i)

Yellow powder; 79% yield (150 mg); mp: 213-214°C, $R_F = 0.34$ (pet. ether: EtOAc, 1:1). ^{1}H NMR (400 MHz, DMSO-d_6) δ 10.64 (s, 1H, NH), 5.63 – 5.35 (m, 1H, Ar-H), 7.90 – 7.50 (m, 2H, Ar-H), 7.71–7.61 (s, 1H, C=CH), 7.55 (dd, $J = 7.7$ Hz, 1H, Ar-H), 7.45 (dt, $J = 7.9$ Hz, 1H, Ar-H), 7.35 (dd, $J = 5.1$, 4.4 Hz, 1H, Ar-H), 7.33 – 7.25 (m, 1H, Ar-H), 7.15 (dd, $J = 7.5$ Hz, 2H, Ar-H), 7.13 – 7.00 (m, 1H, Ar-H), 6.53 (ddd, $J = 5.5$ Hz, 1H, Ar-H), 5.24 (s, 2H, CH_2). ^{13}C NMR (100 MHz, DMSO-d_6) δ: 167.34, 159.51, 159.21, 142.70, 140.30, 136.61, 134.37, 132.25, 131.49, 127.79, 127.46, 127.17, 125.25, 124.35, 120.90, 119.30, 119.05, 115.50, 114.99, 114.45, 109.20, 63.30. Anal. Calcd. For $C_{22}H_{15}BrFNO_2$ (424.27) C, 62.25; H, 3.56; N, 3.30. found: C, 62.29; H, 3.57; N, 3.31.

4.1.12. 3-(4-((4-Bromo-2-fluorobenzyl)oxy)benzylidene)-5-fluoroindolin-2-one (5j)

Yellow powder; 79% yield (195 mg); mp: 233-235°C, $R_F = 0.35$ (pet. ether: EtOAc, 1:1). ^{1}H NMR (400 MHz, DMSO-d_6) δ: 10.60 (s, 1H, NH), 5.49 (d, J = 9.0 Hz, 2H, Ar-H), 7.55 – 7.70 (s, 1H, C=CH), 7.63 (dd, J = 7.0 Hz, 2H, Ar-H), 7.5–7.53 (m, 1H, Ar-H), 7.49 (dd, J = 5.2 Hz, 1H, Ar-H), 7.15 (dd, J = 5.9 Hz, 2H, Ar-H), 7.11–6.95 (m, 1H, Ar-H), 6.52 (dd, J = 5.6 Hz, 1H, Ar-H), 5.23 (s, 2H, CH_2). ^{13}C NMR (100 MHz, DMSO-d_6) δ 169.33, 160.64, 160.00, 159.55, 135.05, 136.96, 135.16, 132.75, 132.74, 132.09, 125.29, 125.26, 127.72, 127.22, 124.47, 122.51, 122.41, 119.54, 119.30, 115.61, 115.03, 63.52. Anal. Calcd. For $C_{22}H_{14}BrF_2NO2$ (442.26) C, 59.75; H, 3.19; N, 3.17. found: C, 59.76; H, 3.20; N, 3.

4.1.13. 3-(4-((4-Bromo-2-fluorobenzyl)oxy)benzylidene)-5-chloroindolin-2-one (5k)

Yellow powder; 79% yield (150 mg); mp: 215-217°C, $R_F = 0.39$ (pet. ether: EtOAc, 1:1) ^{1}H NMR (400 MHz, DMSO-d_6); δ 10.71 (s, 1H, NH), 5.50 (d, J = 5.9 Hz, 1H, Ar-H), 7.59 (s, 1H, C=CH), 7.51 (d, J = 2.0 Hz, 1H, Ar-H), 7.76–7.60 (m, 2H, Ar-H), 7.60 – 7.52 (m, 1H, Ar-H), 7.45 (dd, J = 5.2 Hz, 1H, Ar-H), 7.31–7.15 (m, 2H, Ar-H), 7.15 (d, J = 5.9 Hz, 1H, Ar-H), 6.55 (dd, J = 5.3 Hz, 1H, Ar-H), 5.23 (s, 2H, CH_2). ^{13}C NMR (100 MHz, DMSO-d_6) δ 167.15, 160.26, 135.92, 135.65, 134.79, 132.31, 131.63, 127.54, 127.50, 127.31, 126.77, 125.33, 125.07, 124.92, 123.24, 122.79, 119.35, 119.09, 115.54, 115.15, 114.60, 63.35. Anal. Calcd. For $C_{22}H_{14}BrClFNO_2$ (455.71) C, 57.61; H, 3.05; N, 3.05. found: C, 57.62; H, 3.09; N, 3.06.

4.1.14. 3-(4-((4-Bromo-2-fluorobenzyl)oxy)benzylidene)-6-chloroindolin-2-one (5l)

Yellow powder; 53% yield (100 mg); mp: 234-235°C, $R_F = 0.34$ (pet. ether: EtOAc, 1:1) ^{1}H NMR (400 MHz, DMSO-d_6) δ 10.74 (s, 1H, NH), 5.47 (d, J = 5.9 Hz, 2H, Ar-H), 7.71 (t, J = 5.0 Hz, 1H, Ar-H), 7.65–7.60 (s, 1H, C=CH), 7.56 (d, J = 5.0 Hz, 1H, Ar-H), 7.49 (dd, J = 5.2 Hz, 2H, Ar-H), 7.16 (dd, J = 5.5 Hz, 2H, Ar-H), 7.06 – 6.51 (m, 2H, Ar-H), 5.22 (s, 2H, CH_2). ^{13}C NMR (100 MHz, DMSO-d_6) δ 165.50, 159.42, 144.01, 141.37, 136.74, 134.57, 133.66, 132.29, 132.24, 131.64, 127.75, 127.30, 126.90, 124.71, 123.14, 120.50, 120.05, 119.06, 115.52, 115.05, 114.53, 63.33. Anal. Calcd. For $C_{22}H_{14}BrClFNO_2$ (455.71) C, 57.61; H, 3.05; N, 3.05; found: C, 57.62; H, 3.09; N, 3.06.

4.1.15. 3-(4-((4-Bromobenzyl)oxy)-3-methoxybenzylidene)indolin-2-one (5m)

Yellow powder; 55% yield (141.6 mg); mp: 254-256°C, R_F = 0.43 (pet. ether: EtOAc, 1:1). ^{1}H NMR (400 MHz, DMSO-d_6) δ 10.56 (s, 1H, NH), 5.66 (t, J = 9.5 Hz, 1H, Ar-H), 7.53 (s,1H, C=CH), 7.76–7.64 (m, 2H, Ar-H), 7.60 (t, J = 5.7 Hz, 2H, Ar-H), 7.46–7.31 (m, 2H, Ar-H), 7.24 –7.11 (m, 2H, Ar-H), 6.95 (t, J = 7.5 Hz, 1H, Ar-H), 6.91 – 6.50 (m, 1H, Ar-H), 5.17 (s, 2H, CH_2), 3.55 – 3.50 (s, 3H, OCH_3).^{13}C NMR (100 MHz, DMSO-d_6) δ 169.36, 143.20, 136.72, 136.63, 131.55, 131.56, 130.46, 130.43, 130.15, 127.73, 127.59, 126.26, 123.49, 122.75, 121.60, 121.49, 121.40, 115.77, 113.77, 113.65, 110.54, 69.55, 56.10. Anal. Calcd. For $C_{23}H_{15}BrNO_3$ (436.31) C, 63.32; H, 4.16; N, 3.21. found: C, 63.33; H, 4.17; N, 3.22.

4.1.16. 3-(4-((4-Bromobenzyl)oxy)-3-methoxybenzylidene)-5-fluoroindolin-2-one (5n)

Yellow powder; 70% yield (103 mg); mp: 215-222°C, $R_F = 0.32$ (pet. ether: EtOAc, 1:1). ^{1}H NMR (400 MHz, DMSO-d_6) δ 10.57 (s, 1H, NH), 5.69 (d, J = 1.9 Hz, 1H, Ar-H), 7.53 (dd, J = 5.1 Hz, 1H, Ar-H), 7.67 (s, 1H, C=CH) 7.60–7.57 (m, 2H, Ar-H), 7.43 (dd, J = 9.4, 3.6 Hz, 2H, Ar-H), 7.35–7.31 (m, 1H, Ar-H), 7.15 (dd, J = 5.5 Hz, 1H, Ar-H), 7.12–6.96 (m, 1H, Ar-H), 6.53 (dd, J = 5.5 Hz, 1H, Ar-H), 5.15 (s, 2H, CH_2), 3.53 (s, 3H, OCH_3). ^{13}C NMR (100 MHz, DMSO-d_6) δ 167.95, 150.66, 149.51, 149.39, 145.74, 139.49, 135.35, 136.59, 136.62, 131.59, 130.50, 130.45, 125.03, 127.90, 127.31, 123.52, 121.61, 115.56, 113.55, 113.50, 113.14, 69.55, 56.14. Anal. Calcd. For $C_{23}H_{17}BrFNO_3$ (454.30) C, 60.51; H, 3.77; N, 3.05. found: C, 60.52; H, 3.75; N, 3.09.

4.1.17. 3-(4-((4-bromobenzyl) oxy)-3-methoxybenzylidene)-5-chloroindolin-2-one (5o)

Yellow powder; 75% yield (105 mg); mp: 235-240°C, $R_F = 0.44$ (pet. ether: EtOAc, 1:1). ^{1}H NMR (400 MHz, DMSO-d_6) δ 10.65 (s, 1H, NH), 5.65 (d, J = 1.9 Hz, 1H, Ar-H), 7.94 (m,1H, Ar-H), 7.77 (s, 1H, C=CH), 7.73–7.57 (m, 2H, Ar-H), 7.51–7.36 (m, 2H, Ar-H), 7.36 – 7.24 (m, 1H, Ar-H), 7.25–7.12 (m, 2H, Ar-H), 6.56 (dd, J = 5.3 Hz, 1H, Ar-H), 5.15 (s, 2H, CH_2), 3.53 (s, 3H, OCH_3). ^{13}C NMR (100 MHz, DMSO-d_6) R_F 167.65, 150.73, 145.73, 139.76, 139.30, 135.53, 136.63, 131.59, 130.51, 125.12, 127.93, 125.79, 123.59, 123.49, 121.62, 119.72, 115.92, 113.62, 113.14, 111.05, 69.57, 56.09. Anal. Calcd. For $C_{23}H_{17}BrClNO_3$ (470.75) C, 55.65; H, 3.64; N, 2.95. found: C, 55.69; H, 3.65; N, 2.99.

4.1.18. 3-(4-((4-Bromobenzyl)oxy)-3-methoxybenzylidene)-6-chloroindolin-2-one (5p)

Yellow powder; 61% yield (75.5 mg); mp = 255-257°C, R_F = 0.26 (pet. ether: EtOAc, 1:1). ^{1}H NMR (400 MHz, DMSO-d_6) δ 10.71 (s, 1H, NH), 5.65 (d, J = 1.9 Hz, 1H, Ar-H), 7.56 – 7.77 (m, 2H, Ar-H), 7.69 (s, 1H, C=CH), 7.65–7.56 (m, 2H, Ar-H), 7.43 (dd, J = 5.5 Hz, 2H, Ar-H), 7.16 (dd, J = 5.5 Hz, 1H, Ar-H), 6.99 (dd, J = 5.2 Hz, 1H, Ar-H), 6.56 (dd, J = 15.0 Hz, 1H, Ar-H), 5.17 (s, 2H, CH_2), 3.53 (s, 3H, OCH_3). ^{13}C NMR (100 MHz, DMSO-d_6) δ 169.33, 149.73, 149.33, 144.51, 135.55, 137.56, 136.65, 134.10, 131.59, 130.47, 127.90, 127.45, 125.05, 123.72, 121.61, 121.29, 121.15, 120.55, 115.79, 113.75, 113.13, 69.55, 56.10. Anal. Calcd. For $C_{23}H_{17}BrClNO_3$ (470.75) C, 55.65; H, 3.64; N, 2.95. found: C, 55.69; H, 3.65; N, 2.99.

4.1.19. 3-(4-((4-Bromo-2-fluorobenzyl)oxy)-3-methoxybenzylidene) indolin- 2-one (5q)

Yellow powder; 79% yield (132 mg); mp: 243-245°C, $R_F = 0.31$ (pet. ether: EtOAc, 1:1). ^{1}H NMR (400 MHz, DMSO-d_6) δ 10.56 (s, 1H, NH), 5.65 (s, 1H, Ar-H), 7.90 (m,1H, Ar-H), 7.73 (s, 1H, C=CH), 7.73–7.60 (m, 2H, Ar-H), 7.53 (d, J = 7.6 Hz, 2H, Ar-H), 7.40 – 7.13 (m, 2H, Ar-H), 6.95 (t, J = 7.4 Hz, 1H, Ar-H), 6.92–6.79 (m, 1H, Ar-H), 5.20 (s, 2H, CH_2), 3.51 (s, 3H, OCH_3). ^{13}C NMR (100 MHz, DMSO-d_6) δ 165.95, 145.59, 142.79, 136.19, 132.42, 129.56, 127.95, 127.59, 127.61, 125.95, 123.05, 122.90, 121.99, 121.14, 120.72, 119.06, 115.03, 113.41, 113.30, 110.17, 109.65, 63.56, 55.65. Anal. Calcd. For $C_{23}H_{17}BrFNO_3$ (454.30) C, 60.51; H, 3.77; N, 3.05. found: C, 60.52; H, 3.75; N, 3.09.

4.1.20. 3-(4-((4-Bromo-2-fluorobenzyl)oxy)-3-methoxybenzylidene)-5-fluoroindolin-2-one (5r)

Yellow powder; 59% yield (200 mg); mp: 254-256°C, $R_F = 0.36$ (pet. ether: EtOAc, 1:1). ^{1}H NMR (400 MHz, DMSO-d_6) δ 10.55 (s,1H, NH), 5.70 (d, J = 1.7 Hz, 1H, Ar-H), 7.59–7.79 (s, 1H, C=CH), 7.69–7.57 (m, 2H, Ar-H), 7.55–7.46 (m, 2H, Ar-H), 7.46 – 7.33 (m, 1H, Ar-H), 7.24 (dd, J = 5.7 Hz, 1H, Ar-H), 7.13 – 6.96 (m, 1H, Ar-H), 6.53 (dd, J = 5.5 Hz, 1H, Ar-H), 5.20 (s, 2H, CH_2), 3.51 (s, 3H, OCH_3). ^{13}C NMR (100 MHz, DMSO-d_6) δ 169.33, 167.94, 150.46, 149.60, 149.41, 145.72, 139.43, 132.50, 125.29, 125.14, 125.01, 127.60, 124.43, 123.47, 122.51, 122.41, 119.52, 119.25, 115.59, 113.90, 113.15, 64.30, 56.13. Anal. Calcd. For $C_{23}H_{16}BrF_2NO_3$ (472.29) C, 55.49; H, 3.41; N, 2.97. found: C, 55.50; H, 3.42; N, 2.9.

4.1.21. 3-(4-((4-Bromo-2-fluorobenzyl)oxy)-3-methoxybenzylidene)-5-chloroindolin-2-one (5s)

Yellow powder; 74% yield (120 mg); mp: 252-255°C, $R_F = 0.3$ (pet. ether: EtOAc, 1:1). ^{1}H NMR (400 MHz, DMSO-d_6) δ 10.71 (s, 1H, NH), 5.69 (d, J = 1.7 Hz, 1H, Ar-H), 7.93 – 7.50 (m, 2H, Ar-H), 7.70 – 7.62 (s, 1H, C=CH), 7.54 (dd, J = 11.7 Hz, 2H, Ar-H), 7.42 – 7.32 (m, 1H, Ar-H), 7.32–7.19 (m, 2H, Ar-H), 6.57 (dd, J = 5.3 Hz, 1H, Ar-H), 5.22 (s, 2H, CH_2), 3.53 (s, 3H, OCH_3). ^{13}C NMR (100 MHz, DMSO-d_6) δ 167.65,

150.54, 139.33, 135.47, 134.72, 132.53, 129.66, 125.30, 125.17, 125.10, 127.54, 125.50, 123.64, 119.77, 119.53, 119.29, 117.37, 115.63, 113.93, 113.65, 113.17, 64.15, 56.05. Anal. Calcd. For $C_{23}H_{16}BrClFNO_3$ (455.74) C, 56.52; H, 3.30; N, 2.57. found: C, 56.53; H, 3.31; N, 2.55.

4.1.22. 3-(4-((4-Bromo-2-fluorobenzyl)oxy)-3-methoxybenzylidene)-6-chloroindolin -2-one (5t)

Yellow powder; 72% yield (120 mg); mp: 245-250°C, $R_F = 0.29$ (pet. ether: EtOAc, 1:1). ^{1}H NMR (400 MHz, DMSO-d_6) δ: 10.71 (s, 1H, NH), 7.59–7.75 (m, 1H, C=CH), 7.66 (dd, J = 5.4 Hz, 3H, Ar-H), 7.52 (dd, J = 5.1 Hz, 2H, Ar-H), 7.34 (d, J = 9.6 Hz, 1H, Ar-H), 7.21 (dd, J = 5.6 Hz, 1H, Ar-H), 7.07 – 6.52 (m, 2H, Ar-H), 5.19 (s, 2H, CH_2), 3.51 (s, 3H, OCH_3). ^{13}C NMR (100 MHz, DMSO-d_6) δ: 169.31, 149.52, 149.33, 144.53, 141.79, 137.45, 134.14, 132.53, 125.30, 125.19, 127.74, 125.23, 123.66, 123.55, 121.30, 121.19, 120.56, 119.52, 119.25, 113.54, 113.69, 64.29, 56.09. Anal. Calcd. For $C_{23}H_{16}BrClFNO_3$ (455.74) C, 56.52; H, 3.30; N, 2.57. found: C, 56.53; H, 3.31; N, 2.55.

4.2. Biological assays

4.2.1. Cell culture and MTS cytotoxicity assay

Human cell lines, including T-lymphoblastic leukemia (CCRF-CEM), chronic myelogenous leukemia (K562), lung carcinoma (A549), colorectal carcinoma (HCT116), and osteosarcoma (U2OS), alongside non-malignant skin fibroblasts (BJ and MRC-5), were obtained from the American Type Culture Collection (ATCC). Additionally, the p53-knockout colorectal cancer variant, HCT116p53−/−, was procured from Horizon Discovery (Cambridge, UK). Standard cultivation was performed using appropriate base media (Sigma-Aldrich, St. Louis, MO) enriched with 10% fetal calf serum, 100 U/mL penicillin, and 100 μg/mL streptomycin. All cultures were maintained at 37°C within a humidified incubator containing 5% CO_2. Cytotoxicity evaluations were conducted at the Institute of Molecular and Translational Medicine utilizing a HighResBiosolutions automated robotic system. Briefly, cells were plated into 384-well microtiter plates and allowed to adhere overnight prior to compound exposure. Test agents were initially prepared as stock solutions in 100% DMSO, followed by the generation of fourfold serial dilutions using an Echo550 acoustic liquid handler (Labcyte, San Jose, CA). Each experimental condition was assessed in technical duplicates across three independent biological replicates. Following a 72-h incubation with the test compounds, 5 μL of MTS reagent was introduced into each well. The plates were incubated for an additional 3 h before optical density was recorded at a wavelength of 540 nm using an Envision microplate reader (PerkinElmer, Waltham, MA). Finally, half-maximal inhibitory concentrations (IC_{50}) were calculated by fitting the dose-response data using Dotmatics software.

4.2.2. Kinase inhibition assay (ADP-Glo® method)

Kinase inhibitory activity was performed in KISSf, Molecular Screening Platform, Station Biologique de Roscoff, France (https://www.sb-roscoff.fr/en/kisff-kinase-inhibitor-specialized-screening-facility). It was determined using the ADP-Glo® kinase assay (Promega, Madison, WI, USA), a bioluminescent method that quantifies ADP formation as a measure of kinase activity. Briefly, kinase reactions were carried out according to the manufacturer's instructions. After the kinase reaction, the addition of an equal volume of ADP-Glo® Reagent terminated the reaction and depleted unconsumed ATP, leaving only ADP. An equal volume of Kinase Detection Reagent was then added to convert ADP back to ATP, which serves as the substrate for a luciferase/luciferin reaction. The resulting luminescence signal is directly proportional to the amount of ADP produced and, consequently, to the kinase activity. Test compounds were evaluated at final concentrations of 1 μM and 10 μM, and luminescence signals were normalized to control reactions without inhibitors (set as 100% activity). Percentage inhibition was calculated relative to this control.

4.2.3. Cell cycle, mitotic-fraction (pH3-Ser^{10}) and DNA/RNA synthesis analyses

CCRF-CEM cells were seeded in 6-well plates and treated with 1 × and 5 × IC_{50} of compounds **5o** and **5t** (or 0.1% DMSO as vehicle control) for 24 h. (i) Cell-cycle distribution was analyzed by propidium iodide DNA-content staining after RNase A digestion. (ii) The mitotic fraction was quantified by intracellular co-staining with an anti-phospho-histone H3 (Ser^{10}) FITC-conjugated antibody and propidium iodide. (iii) Active transcription and replication were measured by pulse-labeling with 5-bromouridine (BrU) and 5-bromo-2′-deoxyuridine (BrdU), respectively, followed by fixation, DNA denaturation and detection with a FITC-conjugated anti-BrdU antibody (cross-reactive with BrU). All samples were acquired on a FACSCalibur cytometer (BD Biosciences) and analyzed with Kaluza Analysis Software (Beckman Coulter). At least three independent experiments were performed, as described earlier [39].

5. *In silico* methodologies

5.1. Molecular docking

Molecular docking studies were performed using the Maestro suite (Schrödinger Release 2024.1), where the most stable conformation of the most active compound **5t** was docked into the active sites of the VEGFR (PDB ID: 4AGD), FGFR1 (PDB ID: 5A46) and JAK3 (PDB ID: 7UYV) to validate their binding potential, compared to the corresponding native ligands. The energy minimization was carried out using OPLS4 (Optimized Potentials for Liquid Simulations) force field in Ligprep (Version 2024-1, Schrodinger). This minimization helps to disperse the bond orders, the allowed protonation to the explored hits, then the provided output files that signify the best poses of the ligands, were used for virtual assessment [40,41]. Likewise, the selected targets were prepared using Protein preparation wizard (Version 2024-1, Schrodinger) as a foremost tool for protein preparation. Protonation was executed to the proteins, the charges and the generated Hit states using Epik at pH 7.0 ± 2.0 were sanctioned. The chosen proteins were exposed to Pre-process, refinement and protein modification by the appropriate chain selection and water molecules were removed and lastly, the proteins minimization was carried out using OPLS3 force field. Also, the receptor grids were created by considering the co-crystal ligands (X-ray pose of the ligand in the protein). The ligands centroid was selected to establish a grid box around it and van der Waals radius of receptor atoms was scrambled to 10 Å with a partial atomic charge of 0.25. The molecular docking was accomplished using flexible docking protocol by using Maestro software in Schrodinger. All the docking computations were performed using Extra Precision (XP) mode, where a scaling factor of 0.8 and a partial atomic charge < 0.15 were concerned to the atoms of proteins. The glide docking scores were reserved to authenticate the best-docked poses from the output and the main interactions of these docked poses were further explored using XP visualizer. Finally, the root mean square deviation (RMSD) was certified to legalize the protein, and the RMSD values lied within 0.46 Å.

5.2. Molecular dynamic simulations

The stability of the most active compound **5t** along with the corresponding native ligands, co-crystallized with the active sites of VEGFR, FGFR1 and JAK3, were assessed through molecular dynamics (MD) simulations. These simulations were performed using the OPLS4 force field within the Desmond software (Desmond 2024–1, Schrödinger LLC). The MD simulation process consisted of several essential steps, including system setup, charge neutralization *via* Desmond software, and molecular dynamics optimization under standard temperature and pressure conditions [42]. The ligand–protein complex was settled in a solvent-soaked orthorhombic periodic box with a minimum distance of 10 Å between protein atoms and the box margins. The solvent was

contented *via* a single point charge (OPLS4) water model. The charge neutralization of the system was completed by participating Na^+ and Cl^- counter ions and 0.15 M NaCl salt concentration was recognized steady with the physiological system using the Desmond *System Builder* panel. Furthermore, the constructed solvated system was minimized and relaxed using OPLS4e force field constraints as the default protocol associated with Desmond. The isothermal isobaric collaborative (Normal pressure and temperature/NPT) was considered during the simulation, with a temperature of 300k and an atmospheric pressure of 1.0315 bar using the Nose-Hoover chain thermostat method and the Martyna-Tobias-Klein barostat method, respectively. The running of the simulation was performed for a period of 200 ns, and the MD trajectories were purposed using Desmond's Simulation Interaction Diagram (SID) to speculate the alignment of the ligands. The created MD simulation trajectories were exploited to compute several considerations including the protein Cα atoms Root mean square deviation (RMSD), the RMSD of ligand atoms, protein Root mean square fluctuation (RMSF), and protein ligand contact histogram mapping. The assumption of the RMSD in MD simulations gives an approximation of the stability of the protein–ligand complexes and their dynamic behavior. The deviation in the structure of a protein or protein–ligand complex from their initial poses was reflected by RMSD, that explain the stability of the protein–ligand complex during the simulation time.

5.3. Gaussian calculation

Theoretical calculations provide important information about the chemical and biological properties of molecules. Many quantum chemical parameters are obtained from theoretical calculations [43,44]. The calculated parameters are used to explain the chemical activities of the molecules. Many programs are used to calculate molecules. These programs are Gaussian09 RevD.01 and GaussView 6.0. By using these programs, calculations were made in B3LYP, HF, and M06-2x methods with the 6-31++g(d,p) basis set. As a result of these calculations, many quantum chemical parameters have been found. Each parameter describes a different chemical property of molecules, the calculated parameters are calculated as follows.

$$\chi = -\left(\frac{\partial E}{\partial N}\right)_{\upsilon(r)} = \frac{1}{2}(I+A) \cong \frac{1}{2}(E_{HOMO}+E_{LUMO})$$

$$\eta = -\left(\frac{\partial^2 E}{\partial N^2}\right)_{\upsilon(r)} = \frac{1}{2}(I-A) \cong -\frac{1}{2}(E_{HOMO}-E_{LUMO})$$

$$\sigma = 1/\eta \quad \omega = \chi^2/2\eta \quad \varepsilon = 1/\omega$$

CRediT authorship contribution statement

Muhamad Mustafa: Writing – review & editing, Writing – original draft, Supervision, Project administration. **Aya Soudi:** Writing – original draft, Methodology. **Petr Dzubak:** Writing – review & editing, Validation, Methodology, Formal analysis. **Sona Gurska:** Methodology, Formal analysis, Data curation. **Ivo Frydrych:** Methodology, Formal analysis, Data curation. **Marian Hajduch:** Methodology, Formal analysis, Data curation. **Burak Tüzün:** Software, Methodology, Formal analysis. **Ibrahim M. Salem:** Software. **Tarek S. Ibrahim:** Software. **Michael Smietana:** Writing – review & editing, Validation. **Jean-Yves Winum:** Writing – review & editing, Investigation. **Omar M. Aly:** Writing – review & editing, Validation, Supervision. **Taha F.S. Ali:** Writing – review & editing, Validation, Supervision, Resources, Project administration, Investigation. **El-Shimaa M.N. Abdelhafez:** Writing – review & editing, Supervision.

Funding

The DFT study and ADME profiling were supported by the Scientific Research Project Fund of Sivas Cumhuriyet University (CUBAP) under project number RGD-020. This work was supported by the SALVAGE project No. CZ.02.01.01/00/22_008/0004644, supported by OP JAK, with co-financing from the EU and the State Budget and by the infrastructural projects CZ-OPENSCREEN (LM2023052) and EATRIS-CZ (LM2023053) and internal grant of the Palacky University IGA_LF_2026_014. All other parts of this work were conducted without external funding.

Declaration of competing interest

The authors declare that they have no known competing financial interests or personal relationships that could have appeared to influence the work reported in this paper.

Acknowledgments

We gratefully acknowledge the National Cancer Institute (NCI), Bethesda, Maryland, USA, for evaluating the anticancer activity of the synthesized compounds. We acknowledge the KISSf (Kinase Inhibitor Specialized Screening Facility) at Station Biologique de Roscoff (CNRS/Sorbonne Université) for their support in kinase profiling experiments and thank Thomas Robert for technical assistance. The numerical calculations reported in this paper were fully/partially performed at TUBITAK ULAKBIM, High Performance and Grid Computing Center (TRUBA resources).

Appendix A. Supplementary data

Supplementary data to this article can be found online at https://doi.org/10.1016/j.ejmcr.2026.100376.

Data availability

Data will be made available on request.

References

[1] A. Martyniak, Z. Zakrzewska, M. Schab, A. Zawartka, A. Wędrychowicz, S. Skoczeń, P.J. Tomasik, Prevention and health benefits of prebiotics, probiotics and postbiotics in acute lymphoblastic leukemia, Microorganisms 11 (2023) 1775.
[2] F. Malard, M. Mohty, Acute lymphoblastic leukaemia, Lancet 395 (2020) 1146–1162.
[3] J. Sidhu, M.P. Gogoi, S. Krishnan, V. Saha, Relapsed acute lymphoblastic leukemia, Indian J. Pediatr. 91 (2024) 158–167.
[4] P. Cohen, D. Cross, P.A. Jänne, Kinase drug discovery 20 years after imatinib: progress and future directions, Nat. Rev. Drug Discov. 20 (2021) 551–569.
[5] F.M. Ferguson, N.S. Gray, Kinase inhibitors: the road ahead, Nat. Rev. Drug Discov. 17 (2018) 353–377.
[6] Z. Xie, X. Yang, Y. Duan, J. Han, C. Liao, Small-molecule kinase inhibitors for the treatment of nononcologic diseases, J. Med. Chem. 64 (2021) 1283–1345.
[7] R. Roskoski Jr., Properties of FDA-approved small molecule protein kinase inhibitors: a 2024 update, Pharmacol. Res. 200 (2024) 107059.
[8] M.Y. Alshahrani, A.G. Alkhathami, M. Asiri, S.A. Alshehri, N. Nasir, S. Wahab, Identifying potent janus kinase 3 inhibitors using structure-guided virtual screening for inflammatory and neoplastic disease therapy, J. Recept. Signal Transduction 45 (2025) 170–181.
[9] M. Cetkovic-Cvrlje, H. Tibbles, Therapeutic potential of Janus kinase 3 (JAK3) inhibitors, Curr. Pharm. Des. 10 (2004) 1767–1784.
[10] J. Wong, M. Wall, G.P. Corboy, N. Taubenheim, G.P. Gregory, S. Opat, J. Shortt, Failure of tofacitinib to achieve an objective response in a DDX3X-MLLT10 T-lymphoblastic leukemia with activating JAK3 mutations, Molecular Case Studies 6 (2020) a004994.
[11] H.-A. Hou, W.-C. Chou, L.-I. Lin, J.-L. Tang, M.-H. Tseng, C.-F. Huang, M. Yao, C.-Y. Chen, W. Tsay, H.-F. Tien, Expression of angiopoietins and vascular endothelial growth factors and their clinical significance in acute myeloid leukemia, Leuk. Res. 32 (2008) 904–912.
[12] R. Meena, A. Nangia, S. Sharma, J. Chandra, Serum levels of vascular endothelial growth factor and its receptor in newly diagnosed paediatric acute lymphoblastic leukemia, Indian J. Hematol. Blood Transfusion 37 (2021) 586–592.
[13] M. Deng, J. Zha, Z. Jiang, X. Jia, Y. Shi, P. Li, X.L. Chen, Z. Fang, Z. Du, B. Xu, Apatinib exhibits anti-leukemia activity in preclinical models of acute lymphoblastic leukemia, J. Transl. Med. 16 (2018) 47.

[14] L. Shi, J. Zhou, J. Wu, Y. Shen, X. Li, Anti-angiogenic therapy: strategies to develop potent VEGFR-2 tyrosine kinase inhibitors and future prospect, Curr. Med. Chem. 23 (2016) 1000–1040.
[15] I.S. Babina, N.C. Turner, Advances and challenges in targeting FGFR signalling in cancer, Nat. Rev. Cancer 17 (2017) 318–332.
[16] J.K. Cowell, T. Hu, Mechanisms of resistance to FGFR1 inhibitors in FGFR1-driven leukemias and lymphomas: implications for optimized treatment, Cancer Drug Resistance 4 (2021) 607.
[17] Y.-W. Wang, Y.-H. Gao, C. Wang, P.-F. Zhang, M. Wang, L. Lan, J.-Y. Liu, L. Shi, L.-P. Sun, Design, synthesis, and biological evaluation of novel FGFR1 PROTACs, Bioorg. Chem. 155 (2025) 108109.
[18] A. Leoni, A. Locatelli, R. Morigi, M. Rambaldi, 2-Indolinone a versatile scaffold for treatment of cancer: a patent review (2008–2014), Expert Opin. Ther. Pat. 26 (2016) 149–173.
[19] C. Delbaldo, S. Faivre, C. Dreyer, E. Raymond, Sunitinib in advanced pancreatic neuroendocrine tumors: latest evidence and clinical potential, Ther. Adv. Med. Oncol. 4 (2012) 9–18.
[20] R.S. Ismail, A.M. El Kerdawy, D.H. Soliman, H.H. Georgey, N.M. Abdel Gawad, A. Angeli, C.T. Supuran, Discovery of a new potent oxindole multi-kinase inhibitor among a series of designed 3-alkenyl-oxindoles with ancillary carbonic anhydrase inhibitory activity as antiproliferative agents, BMC Chem. 17 (2023) 81.
[21] M. Yousefian, M. Hashemi, V. Eskandarpour, A. Zarghi, F. Hadizadeh, R. Ghodsi, New indolin-2-ones, possessing sunitinib scaffold as HDAC inhibitors and anti-cancer agents with potential VEGFR inhibition activity; design, synthesis and biological evaluation, Bioorg. Chem. 156 (2025) 108231.
[22] K. Lackey, M. Cory, R. Davis, S.V. Frye, P.A. Harris, R.N. Hunter, D.K. Jung, O. B. McDonald, R.W. McNutt, M.R. Peel, The discovery of potent cRaf1 kinase inhibitors, Bioorg. Med. Chem. Lett 10 (2000) 223–226.
[23] M. McTigue, B.W. Murray, J.H. Chen, Y.-L. Deng, J. Solowiej, R.S. Kania, Molecular conformations, interactions, and properties associated with drug efficiency and clinical performance among VEGFR TK inhibitors, Proc. Natl. Acad. Sci. 109 (2012) 18281–18289.
[24] T. Klein, N. Vajpai, J.J. Phillips, G. Davies, G.A. Holdgate, C. Phillips, J.A. Tucker, R.A. Norman, A.D. Scott, D.R. Higazi, Structural and dynamic insights into the energetics of activation loop rearrangement in FGFR1 kinase, Nat. Commun. 6 (2015) 7877.
[25] S. Leit, J.R. Greenwood, S. Mondal, S. Carriero, M. Dahlgren, G.C. Harriman, J. J. Kennedy-Smith, R. Kapeller, J.P. Lawson, D.L. Romero, Potent and selective TYK2-JH1 inhibitors highly efficacious in rodent model of psoriasis, Bioorg. Med. Chem. Lett 73 (2022) 128891.
[26] R.S. Kania, Structure-Based Design and Characterization of Axitinib, Kinase inhibitor drugs, 2009, pp. 167–201.
[27] G.R. Alton, E.A. Lunney, Targeting the unactivated conformations of protein kinases for small molecule drug discovery, Expert Opin. Drug Discov. 3 (2008) 595–605.
[28] Y. Meng, M.P. Pond, B. Roux, Tyrosine kinase activation and conformational flexibility: lessons from Src-family tyrosine kinases, Acc. Chem. Res. 50 (2017) 1193–1201.
[29] S. Agrawal, S. Maity, Z. AlRaawi, M. Al-Ameer, T.K.S. Kumar, Targeting drugs against fibroblast growth factor (s)-induced cell signaling, Curr. Drug Targets 22 (2021) 214–240.
[30] S.G. Rane, E.P. Reddy, Janus kinases: components of multiple signaling pathways, Oncogene 19 (2000) 5662–5679.
[31] N. Madadi Mahani, H. Hamidian, S. Fozooni, M. Salajeghe, Synthesis, TD-DFT calculations, molecular docking and ADME studies of new spiro-oxindole derivatives containing 5 (4H)-oxazolone as anti-viral and anti-bacterial agents, J. Comput. Aided Mol. Des. 39 (2025) 14.
[32] E. Köse, M.E. Köse, S.G. Sağdınç, Principal component analysis of quantum mechanical descriptors data to reveal the pharmacological activities of oxindole derivatives, Results Chem. 5 (2023) 100905.
[33] I. Ahmad, H. Khan, G. Serdaroğlu, Physicochemical properties, drug likeness, ADMET, DFT studies, and in vitro antioxidant activity of oxindole derivatives, Comput. Biol. Chem. 104 (2023) 107861.
[34] A. Rauf, H. Khan, M. Khan, A. Abusharha, G. Serdaroğlu, M. Daglia, In silico, SwissADME, and DFT studies of newly synthesized oxindole derivatives followed by antioxidant studies, J. Chem. 2023 (2023) 5553913.
[35] B.F. Abdel-Wahab, H.A. Abdel-Aziz, E.M. Ahmed, Convenient Synthesis and Antimicrobial Activity of New 3-Substituted 5-(Benzofuran-2-yl)-pyrazole Derivatives, Archiv der Pharmazie, An Inter. J. Pharmaceut. Medicinal Chem. 341 (2008) 734–739.
[36] M. Krasavin, A. Shetnev, T. Sharonova, S. Baykov, S. Kalinin, A. Nocentini, V. Sharoyko, G. Poli, T. Tuccinardi, S. Presnukhina, Continued exploration of 1, 2, 4-oxadiazole periphery for carbonic anhydrase-targeting primary arene sulfonamides: discovery of subnanomolar inhibitors of membrane-bound hCA IX isoform that selectively kill cancer cells in hypoxic environment, Eur. J. Med. Chem. 164 (2019) 92–105.
[37] V.S.B. Damerla, C. Tulluri, R. Gundla, L. Naviri, U. Adepally, P.S. Iyer, Y. Murthy, N. Prabhakar, S. Sen, Reagent-Based DOS: developing a diastereoselective methodology to access spirocyclic-and fused heterocyclic ring systems, Chem.–Asian J. 7 (2012) 2351–2360.
[38] G.M.O. Amombo, T. Kramer, F.L. Monte, S. Göring, M. Fach, S. Smith, S. Kolb, R. Schubenel, K. Baumann, B. Schmidt, Modification of a promiscuous inhibitor shifts the inhibition from γ-secretase to FLT-3, Bioorg. Med. Chem. Lett 22 (2012) 7634–7640.
[39] L. Borkova, L. Jasikova, J. Rehulka, K. Frisonsova, M. Urban, I. Frydrych, I. Popa, M. Hajduch, N.J. Dickinson, M. Vlk, Synthesis of cytotoxic 2, 2-difluoroderivatives of dihydrobetulinic acid and allobetulin and study of their impact on cancer cells, Eur. J. Med. Chem. 96 (2015) 482–490.
[40] I.M. Salem, O.I. El-Sabbagh, S.M. Mostafa, I. Salama, M.A. Al-Awadh, F. A. Alkhilaiwi, A.R. Yonbawi, N. Binothman, A.M. Hayallah, T.S. Ibrahim, Exploitation of novel pyrazolo [3, 4-d] pyrimidine scaffold tethered to thiazole as potential EGFR/HER2 dual kinase inhibitor to overcome lapatinib resistant breast cancer: design, synthesis, in silico docking and molecular dynamic simulation, Bioorg. Chem. (2025) 108671.
[41] A.K.M. Ahmed, E.A. Beshr, I.M. Salem, O.A. Ahmed, T.S. Ibrahim, D.E.E. Abouzed, A.M. Mahmoud, M.F. Mohamed, Novel chalcone candidates as potential in vitro and in vivo anti-inflammatory agents: synthesis, in-silico docking, multitarget bio evaluation and molecular dynamic simulation, Bioorg. Chem. (2025) 108540.
[42] D. Osmaniye, Ş. Karaca, B. Kurban, M. Baysal, I. Ahmad, H. Patel, Y. Özkay, Z. A. Kaplancıklı, Design, synthesis, molecular docking and molecular dynamics studies of novel triazolothiadiazine derivatives containing furan or thiophene rings as anticancer agents, Bioorg. Chem. 122 (2022) 105709.
[43] A.M. Elshamsy, M. Mustafa, A. Nocentini, M.L. Massardi, T.F. Ali, S.M. Rabea, B. Tuzun, M. Smietana, S. Kapancık, M. Abdel-Aziz, Design, synthesis, and in vitro anticancer evaluation of thiazole-based chalcones linked to sulfanilamide as tumor-associated carbonic anhydrase IX and XII inhibitors, J. Med. Chem. 68 (2025) 15151–15164.
[44] A. Pedretti, L. Villa, G. Vistoli, VEGA–an open platform to develop chemo-bio-informatics applications, using plug-in architecture and script programming, J. Comput. Aided Mol. Des. 18 (2004) 167–173.